fluids

MDPI

Article

Assessing Pedestrian Comfort in Dense Urban Areas Using CFD Simulations: A Study on Wind Angle and Building Height Variations

Paulo Ulisses da Silva [1], Gustavo Bono [2,*] and Marcelo Greco [1]

[1] Programa de Pós-Graduação em Engenharia de Estruturas, Universidade Federal de Minas Gerais—UFMG, Belo Horizonte 31270-901, MG, Brazil; pauloulisses@ufmg.br (P.U.d.S.); mgreco@dees.ufmg.br (M.G.)
[2] Núcleo de Tecnologia, Universidade Federal de Pernambuco—UFPE, Caruaru 50104-900, PE, Brazil
* Correspondence: gustavo.bono@ufpe.br

Abstract

Pedestrian wind comfort is a critical factor in the design of sustainable and livable dense urban areas. This study systematically investigates the effects of surrounding building height and wind incidence angle on pedestrian-level wind conditions, analyzing a nine-building arrangement through validated Computational Fluid Dynamics (CFD) simulations. Scenarios included neighborhood heights varying from 0L to 6L and wind angles from 0° to 45°. The results reveal that wind angles aligned with urban canyons (0° case) induce a strong Venturi effect, creating hazardous conditions with Mean Velocity Ratio (MVR) peaks reaching 3.42. Conversely, an oblique 45° angle mitigates high speeds by promoting flow recirculation. While increasing neighborhood height generally intensifies channeling, the study also highlights that even an isolated building (0L case) can generate hazardous localized velocities due to flow separation around its corners. The Overall Mean Velocity Ratio (OMVR) analysis identifies that, among the studied cases, a 2L neighborhood height is the most tolerable configuration, striking a balance between sheltering and channeling effects. Ultimately, these findings highlight for urban planners the importance of analyzing diverse geometric configurations and wind scenarios, reinforcing the value of CFD as an essential tool for designing safer and more comfortable public spaces.

Keywords: CFD; RANS; pedestrian comfort; wind comfort; building configuration

check for updates

Academic Editors: Liércio André Isoldi, Luiz Alberto Oliveira Rocha, Elizaldo Domingues Dos Santos and Zheng-Tong Xie

Received: 4 July 2025
Revised: 9 August 2025
Accepted: 29 August 2025
Published: 1 September 2025

Citation: Silva, P.U.d.; Bono, G.; Greco, M. Assessing Pedestrian Comfort in Dense Urban Areas Using CFD Simulations: A Study on Wind Angle and Building Height Variations. *Fluids* **2025**, *10*, 233. https://doi.org/10.3390/fluids10090233

Copyright: © 2025 by the authors. Licensee MDPI, Basel, Switzerland. This article is an open access article distributed under the terms and conditions of the Creative Commons Attribution (CC BY) license (https://creativecommons.org/licenses/by/4.0/).

1. Introduction

Global population growth has introduced new challenges for urban planning. The COVID-19 pandemic, during which many regions imposed restrictions on public spaces, highlighted the critical role of shared environments in supporting mental health [1,2]. Beyond these social and psychological dimensions, urban planning must also address pressing environmental issues. Among these, the intensification of thermal discomfort, driven by the Urban Heat Island (UHI) effect, stands out. This phenomenon arises from the predominance of impermeable surfaces and limited vegetation, leading to elevated temperatures in urban centers. According to the Royal Meteorological Society [3], the UHI effect is most pronounced in densely built central areas, as shown in Figure 1a. Additionally, urban morphology strongly influences the dispersion of atmospheric pollutants. For instance, pollutant buildup often occurs in street canyons (narrow roads flanked by tall buildings) heightening exposure to vehicular and industrial emissions. Acoustic pollution also remains a significant concern, with noise levels intensified near major traffic corridors

or industrial zones, contributing to negative health outcomes. Figure 1 summarizes these key urban conditions that contribute to human discomfort. Well-designed urban spaces promote idea exchange, scientific advancement, and social interaction. Accordingly, professionals in architecture, engineering, and urban planning are encouraged to prioritize the integration and improvement of public spaces within buildings, residential complexes and neighborhoods.

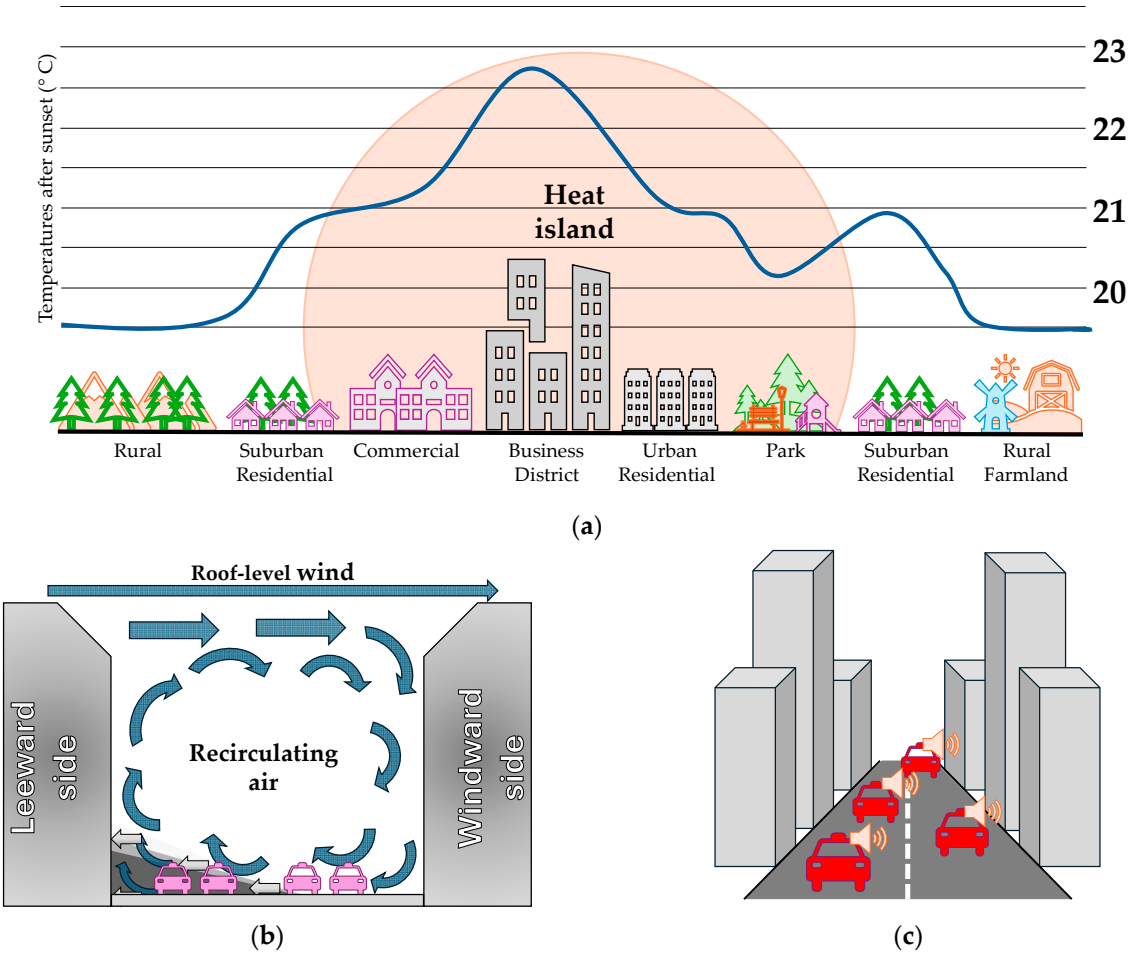


Figure 1. Urban discomfort: (**a**) profile of a typical heat island effect in England; (**b**) pollutant dispersion in a street canyon; (**c**) acoustic contamination of densely built areas.

Among the various criteria influencing the effectiveness of public spaces in urban environments, pedestrian comfort (particularly regarding wind effects) plays a significant role. Excessive wind speeds in densely built areas can pose safety risks to pedestrians and compromise building facades. Liu et al. [4] investigated the impact of large skyscrapers on pedestrian wind comfort and safety, reporting increases in average wind speed and gust intensity, providing comprehension for the development of urban guidelines for tall structures. Hashemi et al. [5] combined Computational Fluid Dynamics (CFD) and field surveys to assess wind comfort and safety at Auckland University of Technology, demonstrating that street orientation and building geometry significantly affect local wind conditions. Liu et al. [6] analyzed wind comfort on external platforms of mega-tall buildings using both wind tunnel experiments and CFD simulations, emphasizing that aerodynamic design strategies can enhance user comfort, while also acknowledging the need for further methodological refinement.

Empirical studies indicate that strong wind exposure reduces the frequency of visits to commercial and public buildings, leading to a diminished urban functionality and

adverse socioeconomic effects on local businesses. Addressing this issue, Shi et al. [7] highlighted the importance of evaluating wind conditions during the urban planning phase, particularly in commercial zones. Their findings suggest that thermal comfort and urban ventilation (typically overlooked in existing standards) contribute meaningfully to the design of more comfortable and safer pedestrian spaces. Chen and Mak [8] used CFD simulations to examine the combined effects of building height and upstream obstructions on thermal and wind comfort, showing that increased height and staggered arrangements improve airflow conditions. Du et al. [9] evaluated pedestrian-level wind comfort under multiple building configurations and wind directions, confirming that "lift-up" designs enhance comfort in both elevated and adjacent areas, especially under oblique wind flows. To address computational efficiency, Nevers et al. [10] incorporated Forchheimer loss terms, enabling neighborhood-scale simulations at reduced computational cost.

The evaluation of thermal and wind comfort for pedestrians and building occupants relies on established methodologies in urban wind engineering. Three principal approaches are commonly employed: (i) in situ measurements using environmental sensors such as anemometers; (ii) physical testing in reduced-scale wind tunnels; and (iii) numerical simulations via CFD. In situ measurements offer high accuracy by capturing real-world environmental conditions and enabling continuous data acquisition over extended periods. However, they involve substantial operational costs, extended deployment times, limited spatial resolution, dependence on specific meteorological conditions, and often require integration with geographic information systems [11,12]. Wind tunnel experiments allow for the controlled simulation of complex aerodynamic interactions but are constrained by the high cost of model fabrication, challenges in replicating realistic flow conditions, and the time-intensive nature of experimental setup [13].

CFD simulations provide operational flexibility and enable detailed analysis of various fluid dynamic parameters, including mean velocity and pressure distribution, Turbulent Kinetic Energy (TKE), and vorticity. They also present a cost-effective alternative to field measurements and physical testing. Nonetheless, the reliability of CFD results depends on the appropriate selection of turbulence models, precise definition of boundary conditions and domain inputs, and the availability of experimental data for validation. High-fidelity simulations further require significant computational resources [14].

Evaluating pedestrian comfort in urban environments involves addressing both thermal and mechanical aspects, the latter related to the direct aerodynamic impact of wind. Both domains are extensively covered in the literature. While studies on thermal comfort incorporate multiple variables (such as air temperature, solar radiation, humidity, and wind speed) in an integrated manner [15–17], assessments focusing on critical wind conditions often prioritize direct aerodynamic effects. Since the primary objective of this study is to investigate potentially hazardous wind flow regimes within urban configurations (such as strong channeling and boundary layer separation) this analysis focuses specifically on kinematic flow parameters [18] that characterize wind intensity. These include the identification of vortical structures, TKE Fields, and velocity-based metrics.

In this study, the Mean Velocity Ratio (MVR) and the Overall Mean Velocity Ratio (OMVR) are adopted as evaluation metrics to quantify pedestrian-scale wind comfort within an urban configuration composed of nine square-plan buildings with a characteristic dimension L. Additionally, the aerodynamic phenomena of TKE, its dissipation, and vorticity are briefly examined to assess their potential influence on the evaluated pedestrian comfort metrics. The arrangement features a central building with height 6L, surrounded by eight peripheral buildings with heights varying from 0L (isolated building scenario) to 6L (uniform urban canyon scenario). Additionally, the effect of wind incidence angle is evaluated in 15° increments from 0° to 45°. CFD simulations are performed using

OpenFOAM to examine how building height and wind direction influence pedestrian-level wind conditions.

The paper is structured as follows: Section 2 reviews the fundamentals of urban wind engineering and established metrics for pedestrian comfort assessment. Section 3 outlines the methodology, including mathematical formulations and numerical schemes. Section 4 presents numerical validation through comparison with experimental data. Sections 5 and 6 provide the discussion of results and concluding remarks, respectively.

2. Literature Review

CFD is a numerical methodology for simulating fluid flow, heat transfer, and related physical phenomena by solving the governing equations of motion. Its application in urban environments has enabled substantial progress in understanding airflow behavior in complex geometries, where experimental methods often face inherent limitations [19]. CFD offers several advantages, including the following:

- Lower costs compared to experimental approaches;
- Scalability across diverse urban configurations;
- High spatial and temporal resolution in flow field predictions.

Owing to these features, CFD has been extensively applied in engineering fields such as wind energy assessment, atmospheric pollutant dispersion modeling, urban microclimate analysis, and evaluation of pedestrian wind comfort. This section reviews the application of CFD in urban wind engineering, with emphasis on neighboring aerodynamic interactions and the established metrics used to quantify pedestrian comfort.

2.1. CFD in Urban Environment and Turbulence Modeling

Urban environments present particularly challenging domains for CFD simulations due to their intricate geometries shaped by buildings and infrastructure, multiscale flow interactions, and the intense turbulence generated by surface features such as buildings, vegetation, ant topography. In this context, turbulence modeling plays a key role in ensuring the reliability of numerical predictions. The most commonly used approaches include the following:

- Reynolds-Averaged Navier–Stokes (RANS) models, which are based on time-averaged formulations of the governing equations;
- Large-Eddy Simulation (LES) models, which resolve large-scale turbulent structures while modeling the smaller scales.

Each modeling strategy involves a trade-off between computational cost and accuracy in representing the complex turbulent behavior of characteristic of urban flows.

RANS models are widely used in engineering due to their low computational cost and ability to predict time-averaged flow characteristics through turbulence closure schemes, primarily the $k-\varepsilon$ and $k-\omega$ models [20–23]. The realizable and Re-Normalization (RNG) variants of the $k-\varepsilon$ model offer improved accuracy in simulating Atmospheric Boundary Layer (ABL) separation, flow recirculation, and building-flow interactions when compared to the standard formulation [24]. For $k-\omega$ models, the Shear Stress Transport (SST) approach is particularly effective in resolving near-wall flows, making it suitable for wind load assessments and pedestrian comfort studies [25]. Additionally, Reynolds Stress Models (RSMs) provide a more detailed representation of anisotropic turbulence by directly solving the transport equations for the Reynolds stresses. However, their increased computational cost and numerical complexity limit their applicability in large-scale urban simulations [26].

Despite the broad use of RANS models in urban studies, their accuracy is inherently constrained by turbulence closure assumptions that do not fully capture complex turbulent

behaviors. For applications requiring higher fidelity (such as detailed flow structures, e.g., vortex shedding, wake dynamics, and turbulence induced by urban features), LES offers a more robust alternative. LES resolves large-scale turbulent structures while modeling the smaller scales through Subgrid-Scale (SGS) models [27], improving the representation of urban turbulence compared to time-averaged RANS approaches. LES has proven effective in capturing transient phenomena in complex three-dimensional flows, including ABL separation, vortex formation in urban canyons, and pollutant dispersion [28]. However, its use is limited by the high computational cost, especially in large domains and under unsteady boundary conditions [29]. As a result, LES is generally applied in scenarios where transient effects and turbulence detail are essential, such as pedestrian wind comfort and pollutant dispersion studies [30–32]. Conversely, RANS remains the preferred approach for steady-state simulations focused on mean velocity fields, including urban wind energy assessments [33–35]. Ultimately, the choice between RANS and LES involves balancing physical accuracy and computational feasibility, with LES often serving as a benchmark for validation RANS predictions, particularly when supported by high-performance computing resources.

CFD has become an essential tool in building aerodynamics, supporting analysis of wind loads, natural ventilation, and urban microclimate modifications [36]. It contributes to optimizing architectural forms and urban layouts for energy efficiency by evaluating how geometries influence flow patterns and wind acceleration [37]. CFD also helps assess the integration of renewable energy systems, such as rooftop wind turbines in complex urban settings [38], promoting more sustainable designs. Best practices highlight the importance of appropriate mesh resolution, turbulence model selection, and validation against experimental data. For example, Vita et al. [39] showed that while LES is preferable for small-scale applications, RANS can provide reliable results when computational resources are limited.

2.2. Neighborhood Effects on the Wind Flow

Urban development introduces increasing complexity to city landscapes in terms of wind engineering and aerodynamic interactions. Variations in flow patterns can substantially affect wind loads on structural systems. The Brazilian standard NBR 6123:2023 [40] includes an approximate neighborhood effect coefficient f_v to adjust aerodynamic coefficients, although it applies only to structural analyses involving two buildings. As such, current regulatory provisions do not fully address more intricate urban configurations, prompting ongoing research into factors such as building height, relative positioning, and wind incidence angles. Changes in urban form influence flow direction and surface roughness, making interference effects critical in design evaluations.

Blessmann [41] identified three key phenomena associated with neighboring structures: hammering, referring to periodic loads generated by von Kármán vortex shedding that induce dynamic responses in downstream structures; the Venturi effect, describing flow acceleration through constricted passages that alter pressure coefficients; and wake turbulence, where buildings closely aligned downstream are shielded from direct wind exposure, resulting in vortex formation in the wake region.

2.3. Criteria for Pedestrian Comfort

A wide range of studies in wind engineering literature propose criteria for evaluating pedestrian comfort in urban environments. Among the most prominent are those by Du et al. [42] and Chen and Mak [43], which examine criteria applied in Hong Kong, a city marked by high population density and urbanization, where pedestrian wind comfort is a

daily concern. Such evaluations contribute to better urban planning, especially in densely built areas where airflow is constrained by tall buildings and narrow corridors.

Traditional pedestrian comfort criteria rely on parameters such as mean wind velocity and the probability of exceeding predefined thresholds. These values are typically associated with human activities (e.g., sitting, walking, running), for which acceptable limits are defined. Most frameworks adopt mean or gust wind speed as threshold parameters, with maximum exceedance probabilities corresponding to varying levels of comfort and safety. However, many of these approaches were initially developed for high-wind environments and may not be well-suited to dense urban areas, where irregular building spacing and reduced ventilation complicate flow–structure interactions.

Du et al. [42] proposed criteria tailored to compact urban environments, particularly under the hot and humid conditions of Hong Kong. A central parameter is the Mean Wind Velocity Ratio (MVR), defined as the ratio between the mean wind speed at pedestrian level and the approaching reference wind speed. For broader assessments involving multiple wind directions and their respective occurrence probabilities, the Overall Mean Wind Velocity Ratio (OMVR) is adopted.

These indices have proven effective in representing and quantifying pedestrian comfort in complex urban contexts and are therefore recommended for studies and policies aimed at improving pedestrian-level wind conditions. Equations (1) and (2) describe how to calculate these indices, while Table 1 presents threshold values for user comfort classification, where U is the velocity at pedestrian level, U_{ref} is the reference wind velocity, and F is the probability of wind from direction i.

$$MVR = \frac{U}{U_{ref}} \tag{1}$$

$$OMVR = \sum_{i=1}^{n} F_i \times MVR_{i,SM} \tag{2}$$

Table 1. MVR and OMVR criteria for pedestrian comfort.

Category	Threshold Wind Velocity (m/s)	MVR	OMVR	Remarks
Unfavorable	<1.5	<0.3	<1.5 U_{ref}	Low wind velocity.
	<1.8	<0.36	<1.8 U_{ref}	
Acceptable	<3.6	<0.72	<3.6 U_{ref}	Moderate wind velocity: good for outdoor activities.
	<5.3	<1.06	<5.3 U_{ref}	
Tolerable	<7.6	<1.52	<7.6 U_{ref}	High wind velocity: not suitable for all outdoors activities.
Intolerable	>7.6	>1.52	>7.6 U_{ref}	Dangerous wind velocity: not suitable for any outdoors activities.
Dangerous	>15	>3	>15 U_{ref}	Hazardous wind velocity.

The values in Table 1 are compiled from references [8,42–44]. It is important to emphasize that selecting appropriate threshold values should also account for local climatic conditions and the probability of wind speed exceedance, as these factors vary with each specific evaluation context.

3. Methodology

This study employed the standard RANS $k-\varepsilon$ turbulence model to simulate turbulent flows, implemented within the OpenFOAM v12 framework, as described in the subsections below. This section presents the main equations for the $k-\varepsilon$ model, along with details of the computational domain and the adopted numerical schemes. The same methodology

and setup are also used and described in Silva et al. [45] to capture wind loads in the central building.

3.1. Turbulence Model

The $k-\varepsilon$ model characterizes turbulence using two transport variables, namely TKE (k) and dissipation rate (ε), based on the formulations of Launder and Spalding [46], Launder et al. [47], and Tahry [48]. From these variables, the turbulent viscosity (ν_t) is computed and applied to close the transport equations of averaged flow quantities. ν_t is calculated using Equation (3), where $C_\mu = 0.09$ is the model coefficient for turbulent viscosity.

$$\nu_t = C_\mu \frac{k^2}{\varepsilon} \tag{3}$$

This implementation in OpenFOAM is appropriate for highly turbulent flows in relatively stable environments, such as simplified urban settings. The transport equations for k and ε are solved alongside the conservation equations of mass and momentum, as shown in Equations (4) and (5). In these equations, $\rho = 1.225$ kg/m^3 represents the air density; D_k is the effective diffusivity for the dissipation rate; $C_1 = 1.44$ and $C_2 = 1.92$ are model constants; and $\boldsymbol{u}$ is the velocity field.

$$\frac{D}{Dt}(\rho k) = \nabla\cdot(\rho D_k \nabla k) + P - \rho\epsilon \tag{4}$$

$$\frac{D}{Dt}(\rho \epsilon) = \nabla\cdot(\rho D_\epsilon \nabla \epsilon) + \frac{C_1 \epsilon}{k}\left(P + C_3 \frac{2}{3} k \nabla\cdot\boldsymbol{u}\right) - C_2 \rho \frac{\epsilon^2}{k} \tag{5}$$

The model assumes local equilibrium between the production and dissipation of TKE in regions distant from solid boundaries. It is recommended for applications where velocity gradients are dominant over separation or recirculation effects, such as in simple geometric configurations used in urban flow studies. The selection of the standard $k-\varepsilon$ model is justified by its robustness, low computational cost, and widespread validation in urban flow and wind load assessments.

3.2. Boundary and Initial Conditions

The computational domain was defined according to established guidelines for simulating flow around building arrays (see Franke et al. [49] and Tominaga et al. [50] for further details). The central building, with B:W:H (base/width/height) proportions, was placed 5H from the inlet and 15H from the outlet, with side distances of 5H from adjacent structures, ensuring symmetry along the central longitudinal plane. The domain height extends up to 5H above the building, as illustrated in Figure 2.

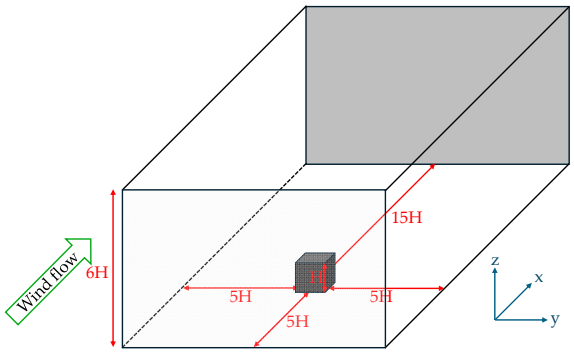


Figure 2. Simulation domain.

The configuration includes eight buildings arranged equidistantly with a spacing of 1B. The ABL was modeled using a classical logarithmic profile suitable for flat terrain, with a roughness length z_0 = 0.0024 m and zero-plane displacement d = 0 m. The reference velocity is u_{ref} = 5 m/s at a height of 1 m. The inlet equations for the velocity profile $u(z)$ and the friction velocity u^* are given in Equations (6) and (7), respectively, where κ = 0.40 is the von Kármán constant.

$$u(z) = \frac{u^*}{\kappa} ln\left(\frac{z - d + z_0}{z_0}\right) \tag{6}$$

$$u^* = \frac{u_{ref}\kappa}{ln\left(\frac{z-d+z_0}{z_0}\right)} \tag{7}$$

The turbulent kinetic energy k and dissipation rate ε were determined using standard ABL formulations, adjusted by the constants presented in Section 3.1, through Equations (8) and (9), respectively.

$$k = \frac{v^*}{\sqrt{C_\mu}} \sqrt{C_1 ln\left(\frac{z - d + z_0}{z_0}\right) + C_2} \tag{8}$$

$$\varepsilon = \frac{(v^*)^3}{\kappa(z - d + z_0)} \sqrt{C_1 ln\left(\frac{z - d + z_0}{z_0}\right) + C_2} \tag{9}$$

At the domain outlet, a homogenous Neumann condition was applied, meaning that the normal gradient of the variables is zero, allowing for flow extrapolation ($\nabla\phi \cdot \boldsymbol{n} = 0$). The lateral and top boundaries were treated as symmetry planes, assuming no flow penetration and no normal gradient of velocity or other variables. The ground and building surfaces were modeled as rough walls using empirical approximations that impose velocity and stress profiles consistent with turbulent flow near solid boundaries. The 3D mesh was generated using the snappyHexMesh utility, which enables progressive refinement around the geometries based on STL files representing the building surfaces.

3.3. Numerical Schemes

A segregated steady-state solution method was adopted for the simulation cases, using incompressible flow solver foamRun—incompressibleFluid. Temporal discretization followed the implicit Euler scheme, which is first-order and non-oscillatory. Although typically associated with transient problems, this time scheme was applied here in a steady-state configuration to enhance numerical stability and robustness, even with relatively large time steps.

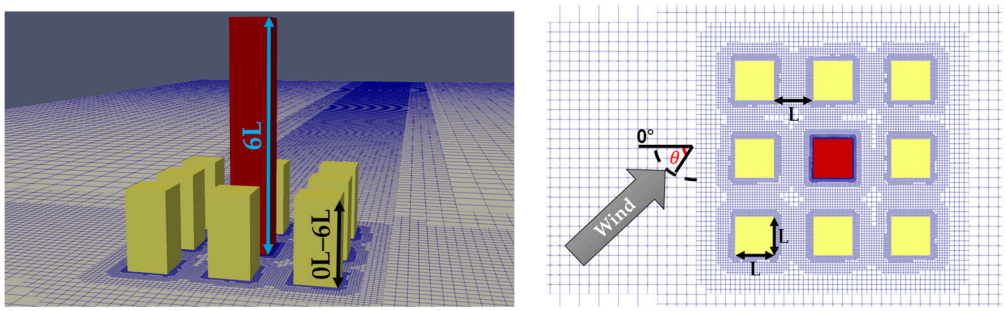
Spatial discretization of gradient terms was carried out using the Gaussian finite volume method with linear interpolation between cell centers. This approach confines extrapolated values at cell interfaces within the range defined by neighboring cells, thus avoiding non-physical oscillations. Divergence terms, related to advection and diffusion, were discretized using the linear upwind Gauss scheme, which improves stability when solving advective and dissipative flows. This discretization strategy was consistently applied to the governing equations for velocity, TKE, and dissipation rate.

Terms involving the Laplacian operator were treated using the linear corrected scheme, which adds orthogonal corrections to address geometric non-orthogonality between cells. The resulting algebraic system was solved using the Geometric Agglomerated Multi-Grid (GAMG) method for pressure, which increases efficiency by leveraging multiple mesh levels. For velocity, TKE, and dissipation fields, the *smoothSolver* was employed. Convergence

criteria included a tolerance of 10^{-6} for all primary variables and 10^{-4} for global residual control. Further details on this methodology can be found in Silva [51].

3.4. Simulation Case

A simplified urban configuration comprising nine buildings was analyzed. The central building, located at the core of the layout, has dimensions of L × L × 6L, where L is the base edge length. The surrounding buildings share the same base dimension L, while their heights vary from 0L (representing an isolated central building) to 6L (all buildings with equal height), in increments of L. In this domain, the physical value of L is 10 cm. The buildings are spaced L apart, as illustrated in Figure 3.



(**a**) (**b**)

Figure 3. Simulation cases: (**a**) perspective view and (**b**) top view.

Pedestrian comfort was evaluated in the four street canyons surrounding the central building, labeled "Streets" #1 to #4, as shown in Figure 4. At each location, the MVR and OMVR metrics were calculated at a height of 0.075L above the ground level, corresponding to the typical height of pedestrian wind exposure. Each building height configuration was examined for four wind incidence angles: θ = 0°, 15°, 30°, and 45°. As the study does not pertain to a specific geographic location, all wind directions were assumed to have equal probabilities of occurrence (F_i = 25%).

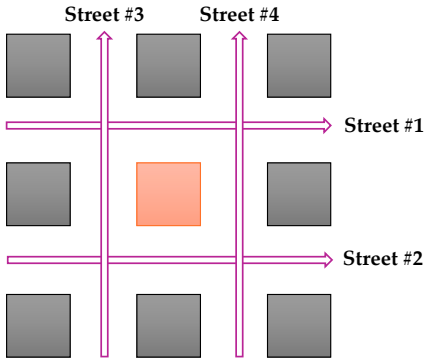


Figure 4. MVR assessment lines.

The computational meshes generated for each case contained approximately 4.7 million finite volumes on average. Simulations were conducted at a Reynolds number of Re = 100,000. The layout was initially designed to enable a systematic and controlled investigation of neighborhood interference on pressure coefficients and wind loads acting on the central building, supporting structural design applications [45]. However, given the availability of this simulation dataset, the current study repurposes it to explore a related aerodynamic phenomenon of urban relevance: the impact of building height variation on pedestrian-level wind comfort. Thus, while the configuration can support analyses related

to tall buildings, the specific objective is to assess how geometric variations in building heights affect airflow within adjacent urban canyons.

3.5. Wall Treatment and Mesh Conditions

The treatment of the boundary layer adjacent to solid structures (buildings and ground) is critical for the accuracy of CFD simulations, especially in capturing velocity gradients and flow separation phenomena. To ensure adequate modeling of this region, the non-dimensional wall distance parameter, y^+, is employed to assess mesh resolution. It is calculated using Equation (10), where y is the distance from the first mesh cell to the wall, and $v = 1.5 \times 10^{-5}$ m^2/s^2 is the kinematic viscosity of air.

$$y^+ = \frac{y \cdot u^*}{v} \tag{10}$$

The RANS $k - \varepsilon$ turbulence model used in this study applies wall functions to represent near-wall flows. While computationally efficient, this approach does not resolve the viscous sublayer directly, requiring the first mesh cell to be located within the logarithmic region of the boundary layer. For valid application of wall functions, y^+ values should ideally lie within the range [30, 300]. However, in the context of wind engineering and high-Reynolds-number flows around tall buildings, smaller y^+ may be required to adequately capture finer-scale effects, as observed in Liu et al. [52] and Liu and Niu [53].

4. Validation

This section presents the validation process for the adopted CFD configuration. A reference benchmark case was used to compare the results obtained in this study. The CFD analyses were conducted using OpenFOAM v12 on a system running Ubuntu 18.04.6 LTS, equipped with an Intel Core i5-4200U processor (dual-core, 1.60 GHz) and 6 GB of RAM.

To verify the OpenFOAM setup and the numerical schemes employed, a benchmark case involving two identical prismatic buildings was simulated. These structures had a geometric ratio of 1:1:4 (width/depth/height), and wind incidence angles of 0°, 15°, 30° and 45° were evaluated, as illustrated in Figure 5.

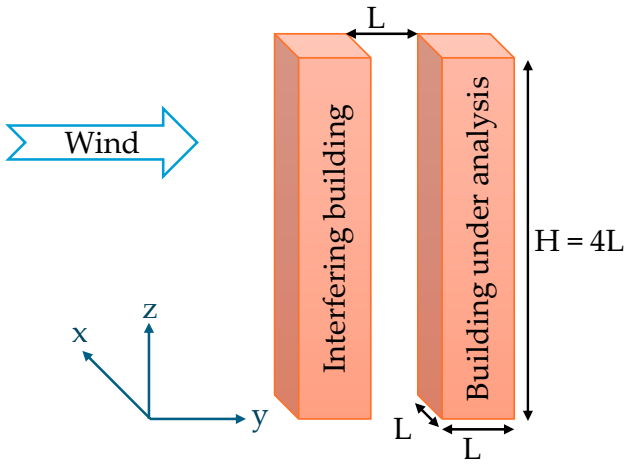
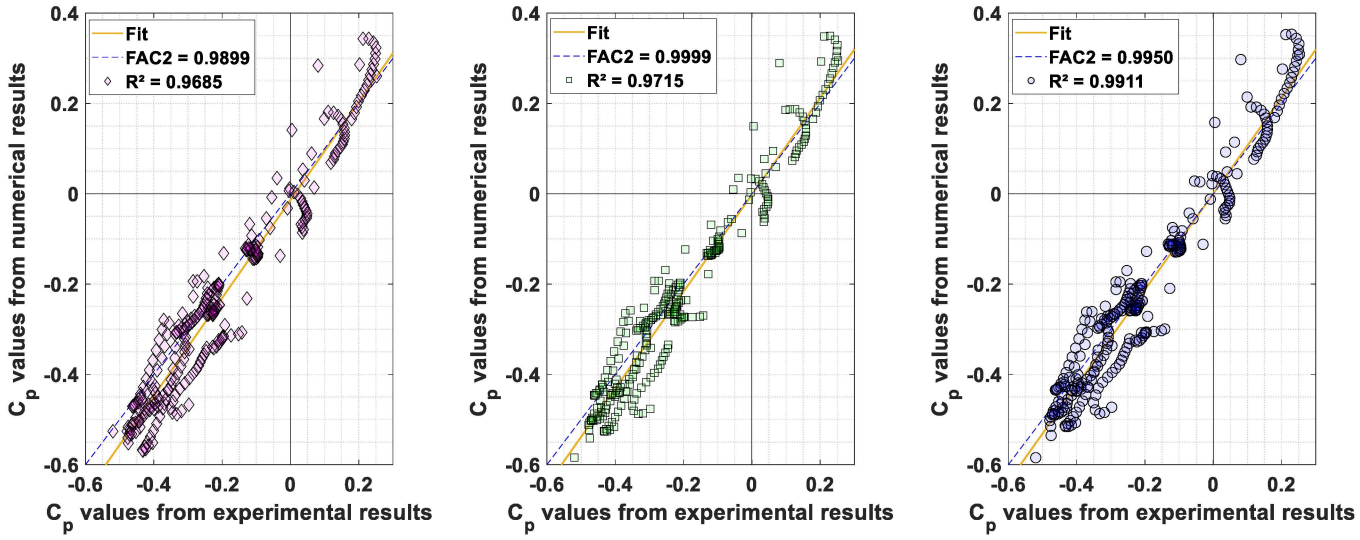


Figure 5. Validation case: side view with wind incidence angle at 0°.

For each wind direction, the mean pressure coefficient C_p was plotted along the symmetry lines of the four façades of the analyzed building. These values were compared to experimental data using scatter plots, with experimental results on the horizontal axis and simulated results on the vertical axis. Five statistical metrics were employed to assess the agreement between simulations and experiments: the coefficient of determination

(R^2), Fractional Bias (FB), the fraction of predictions within a factor of two of observations (FAC2), Root Mean Square Error (RMSE) and Mean Absolute Error (MAE). Higher R^2 and FAC2 values indicate stronger correlation, while lower FB, RMSE, and MAE reflect smaller deviations.

Three mesh refinement levels were tested: M1 (≈375,000 cells), M2 (≈1,428,000 cells), and M3 (≈3,785,000 cells). The results were compared with wind tunnel data from Tokyo Polytechnic University [54]. Figure 6 presents the results for each mesh level, aggregating data from all wind directions, and Table 2 summarizes the statistical metrics and corresponding regression equations.



(**a**) (**b**) (**c**)

Figure 6. Numerical data against experimental data scatter plot: (**a**) M1, (**b**) M2, and (**c**) M3 meshes.

Table 2. Agreement coefficients between experimental data and the three refinement levels.

Mesh	Fit Equation	R^2	FB	FAC2	RMSE	MAE
M1	1.084x − 0.0139	0.9685	0.0430	0.9899	0.0630	0.0525
M2	1.073x − 0.0021	0.9715	0.0896	0.9999	0.0522	0.0444
M3	1.064x + 0.0004	0.9911	0.0160	0.9950	0.0323	0.0257
Average	-	0.9770	0.0495	0.9949	0.0491	0.0409

The level of agreement between simulations and experimental data varied depending on wind direction. In general, finer mesh resolutions led to improved R^2 values. Fractional Bias (FB) was lowest for the finest mesh (M3), indicating mesh convergence. FAC2 values remained comparable across all meshed, suggesting minimal differences in predictive reliability. Exceptions were observed in FB, which increased from M1 to M2 but decreased to its lowest value in M3, and in FAC2, where M2 outperformed M3. Nonetheless, these differences are statistically negligible, as the occurrence of extreme values in refined meshes is a common characteristic of numerical simulations.

Overall, although the $k-\varepsilon$ model tended to overestimate pressure in positive regions and underestimate them in negative zones, it effectively captured wind behavior around urban buildings, including the influence of surrounding structures. These findings support the adequacy of the $k-\varepsilon$ model and validate the use of a mesh resolution equivalent to M3 for the simulations conducted in this study.

5. Results and Discussion

This section presents the results of the MVR criterion for each scenario across the four designated streets. The OMVR parameter is subsequently analyzed for the full neighborhood configuration, covering all four streets and wind directions. For reference, pedestrian-level flow profiles and corresponding MVR plots for each street are provided in Appendix A (Tables A1–A7). For each simulation, the time-averaged wall-distance parameter y^+ is reported, including its minimum, maximum, and average values over the mesh through time. Furthermore, Figures 7–9 provide a comparative overview through bar charts that summarize the findings for each street.

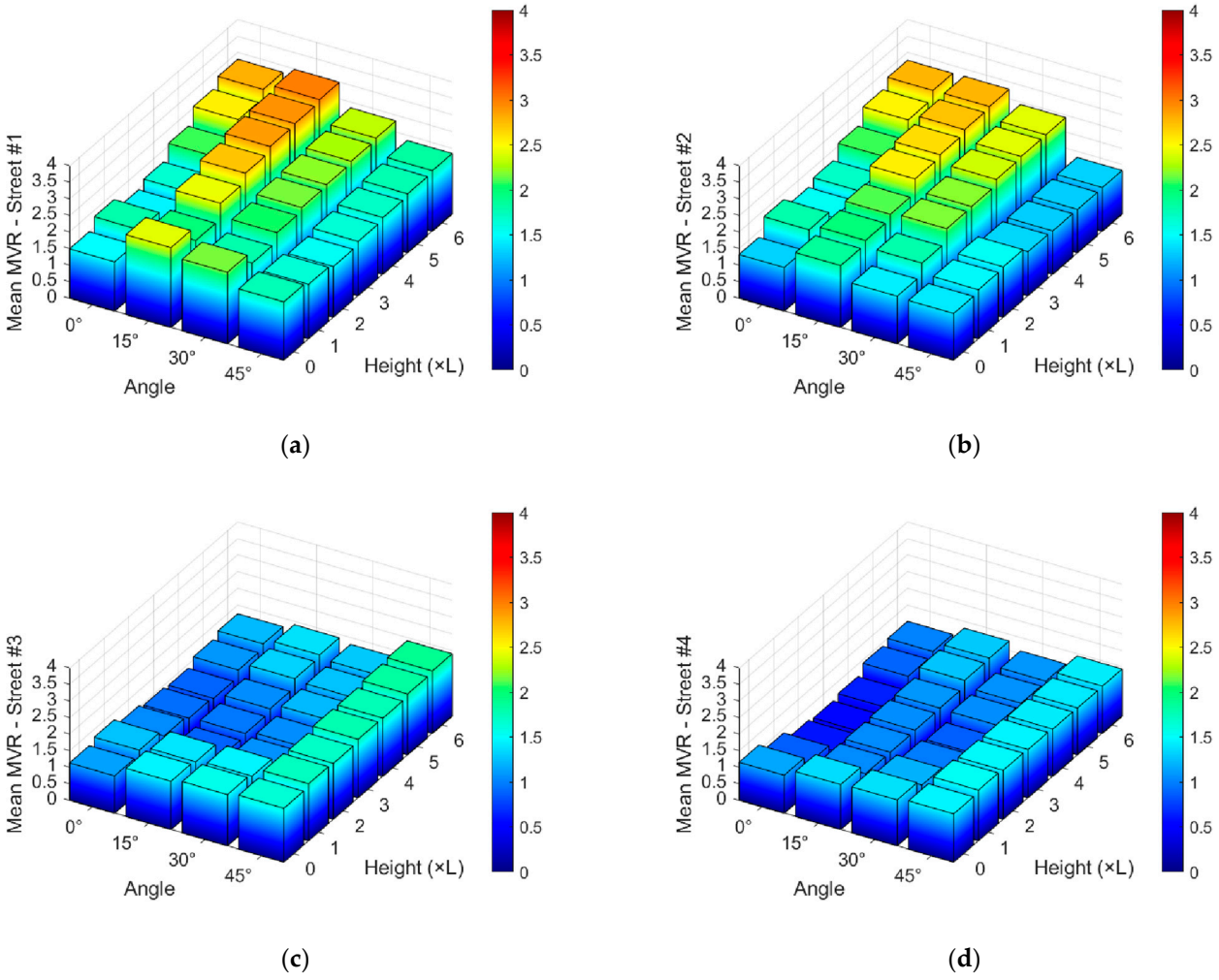


Figure 7. Mean MVR values for (**a**) Street #1, (**b**) Street #2, (**c**) Street #3, and (**d**) Street #4.

5.1. Wind Incidence Angle Analysis

The analysis of the plots reveals that the MVR criterion varies significantly with the wind incidence angle relative to the building layout. Flow profiles in Appendix A show that when the wind approaches the neighborhood at 0°, aligning perfectly with the urban canyons, the Venturi effect becomes highly prominent. This alignment channels the airflow and accelerates wind speed between buildings, with max MVR values peaking at 3.42 for the h = 6L configuration. A similar trend is observed at θ = 15°, where, despite the lack of perfect alignment, the Venturi effect remains dominant, particularly for $h \geq$ 4L. In this case, mean MVR values even surpass those at θ = 0°, reaching 2.99 for h = 6L, due to the combined effects of recirculation and flow acceleration.

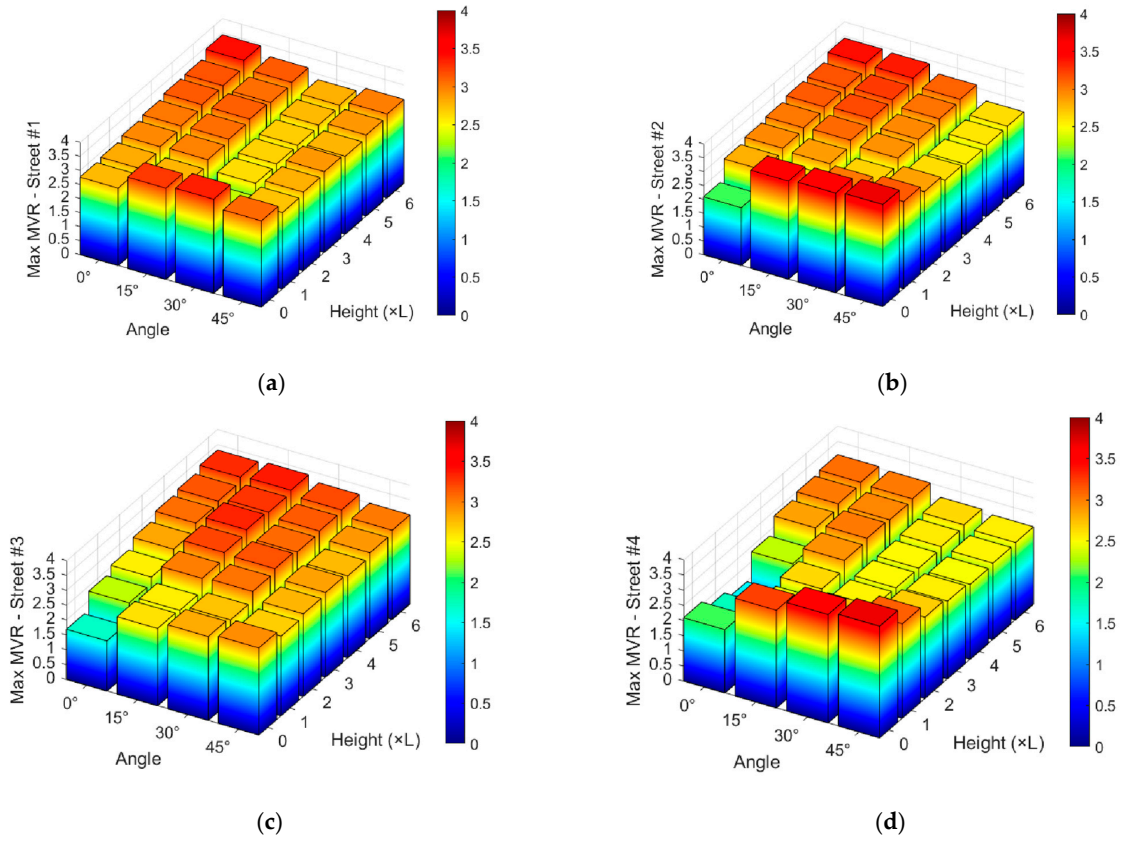


Figure 8. Max MVR values for (**a**) Street #1, (**b**) Street #2, (**c**) Street #3, and (**d**) Street #4.

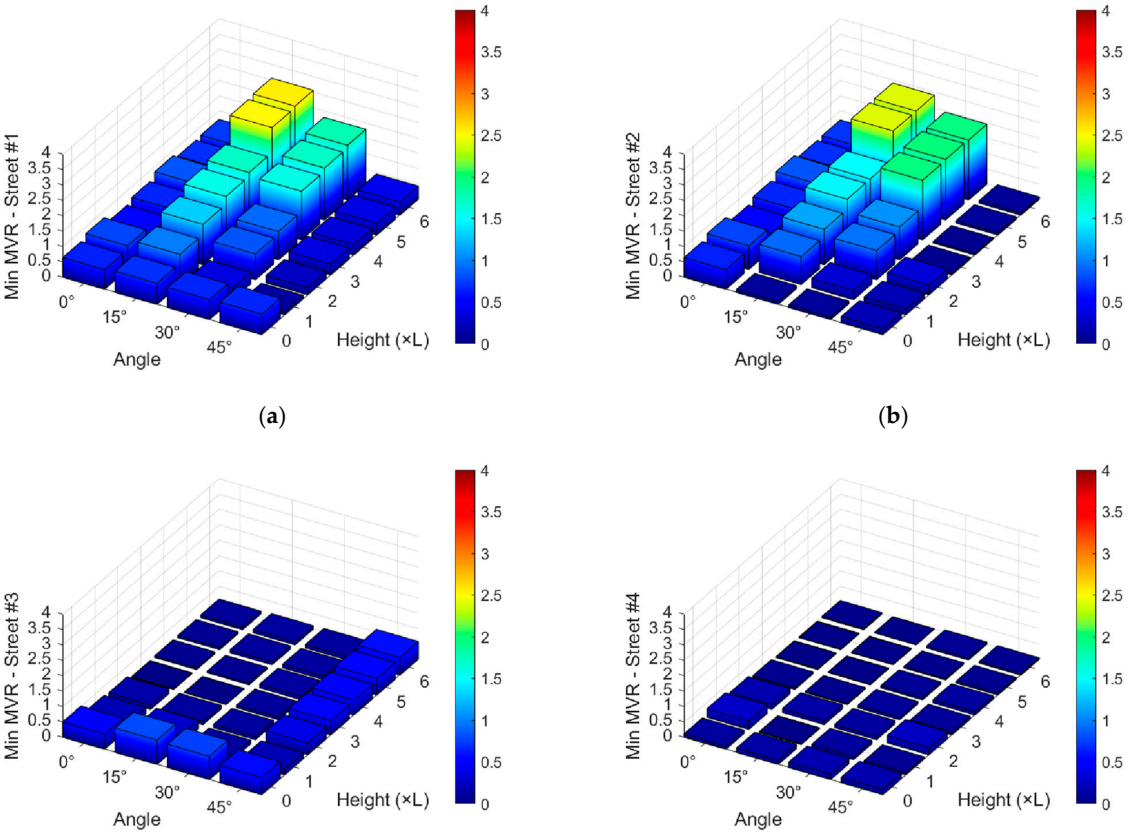


Figure 9. Min MVR values for (**a**) Street #1, (**b**) Street #2, (**c**) Street #3, and (**d**) Street #4.

At $\theta = 30°$, this behavior begins to shift. While the Venturi effect still influences the flow, recirculation becomes the prevailing mechanism, marked by the formation of multiple vortices downstream of the buildings, especially for $h \geq 3L$. As a result, MVR values start to decline compared to those at $\theta = 0°$ and 15°, although critical peaks still occur. Bar charts in Figures 7–9 show a notable reduction in mean MVR values, particularly for Streets #1 and #2, which were previously aligned with the flow, and in max MVR values for Streets #1, #2, and #4.

At $\theta = 45°$, a generalized reduction in MVR values is observed across the canyons. The absence of alignment makes the Venturi effect less influential and recirculation the dominant flow feature. Flow profiles confirm minimal variation across building heights in this case, as the misalignment weakens flow acceleration. The bar charts indicate that $\theta = 45°$ yields the lowest mean, maximum and minimum MVR values: the highest max is 3.14 (at $h = 1L$), and the highest mean is 1.89 (at $h = 6L$).

In summary, flow profiles for 0° and 15° cases show wind being forced through the narrow canyons of Streets #1 and #2. As building height increases, red-colored high-velocity zones become more dominant in the figures, evidence of the Venturi effect. This phenomenon directly causes the hazardous MVR peak of 3.42 observed in Figure 8. In contrast, at $\theta = 45°$, the misaligned flow spreads along the canyons and dissipates TKE throughout the domain, preventing strong wind gusts and promoting vortex formation downstream. This leads to substantially lower MVR values, enhancing pedestrian comfort, as shown in Figures 7 and 8.

5.2. Neighborhood Height Analysis

The influence of neighboring building height on the MVR parameter was initially examined through streamline visualizations, provided in Appendix A. At $h = 1L$, the flow followed multiple trajectories for all wind incidence angles. However, from $h = 3L$ onward, a clear trend emerged: the flow became increasingly channeled within the urban canyons, showing fewer deviations at intersections and a stronger tendency to follow the main wind direction. This behavior was most evident at $\theta = 0°$ and 15°, but also discernible at $\theta = 30°$ and 45°.

From $h = 4L$, the flow assumed a preferential path along the street axes, indicating an intensification of the Venturi effect as the height of surrounding buildings increased. This effect was particularly notable in Streets #1 and #2 at $\theta = 0°$, 15°, and 30°, where flow alignment with the streets favored wind acceleration due to narrowing canyon cross-sections. Initially, MVR plots for these streets showed significant variability between corridor and intersection regions. However, with increasing building height, this variability decreased, while the mean and maximum MVR values increased. Bar charts confirmed this trend: an overall rise in the MVR and a reduction in its variability for canyons aligned with the wind direction, with perpendicular canyons also showing a less pronounced but consistent increase.

The isolated case ($h = 0L$) presented contrasting results. Streamlines revealed significant wind acceleration near the solitary building, while regions farther away retained inlet velocity. This produced localized MVR peaks that in some instances exceed those caused by the Venturi effect. Although this effect was less pronounced at $\theta = 0°$, at $\theta = 15°$ the average MVR along Streets #1 and #2 surpassed those of $h = 1L$ and 2L. High MVR maxima were recorded at $\theta = 15°$, 30°, and 45°, in some cases exceeding the maxima found in $h = 6L$ scenarios. This indicates that while a uniform-height neighborhood leads to higher average MVR, the isolated case can produce more extreme local peaks, potentially causing pedestrian discomfort or safety concerns (MVR values above 3.60 were observed in Streets #3 and #4).

In conclusion, the analysis confirms that surrounding building height significantly affects pedestrian comfort. The isolated building scenario exhibits unique flow behavior: despite lower average MVR values, corner-induced boundary layer separation accelerates flow in its immediate surroundings, producing critical MVR peaks (see Table A1 graphs). These peaks, exceeding 3.60, highlight the potential for hazardous conditions even in sparsely built environments. From h = 3L onward, a clear increase in MVR is observed with building height. From h = 4L, the flow is channeled more efficiently along canyon axes, as illustrated in Tables A5–A7 for $\theta = 0°$ and 15°, where MVR profiles for Streets #1 and #2 become smoother. This progression is quantitatively reinforced in Figure 7, where MVR values consistently rise with surrounding building height, underscoring the dominance of channeling over potential sheltering effects.

5.3. Overall Pedestrian Comfort

Based on the thresholds defined in Table 1, the simulation results reveal that, even under simplified configurations such as the idealized urban arrangement adopted in this study, peak MVR values induced by boundary layer separation and neighborhood effects can generate potentially hazardous wind conditions for pedestrians. These peaks typically occur in narrow passages between aligned buildings, whereas minimum values are generally located at street intersections, where greater cross-sectional areas mitigate wind acceleration.

In all tested scenarios, at least one canyon exhibited peak MVR values above tolerable comfort thresholds, although lower intensities were recorded at $\theta = 45°$, due to reduced alignment between wind and street axes. The simplified configuration favors the development of preferential wind corridors, further intensifying velocities in localized regions.

Despite these peaks, average MVR values remain within acceptable comfort levels for lower building heights. However, as the surrounding buildings become taller, a consistent trend emerges: the mean MVR increases, approaching thresholds indicative of discomfort. This is evidenced in the bar charts, which show a clear upward progression of average MVR with building height.

To account for all wind directions, the OMVR metric (normalized by the reference velocity) is computed assuming uniform directional probability (F_i = 25%) and presented in Figure 10. While real-world evaluations require region-specific wind data, such as those provided by Brazil's National Institute of Meteorology (INMET), this study adopts a hypothetical framework for illustrative purposes.

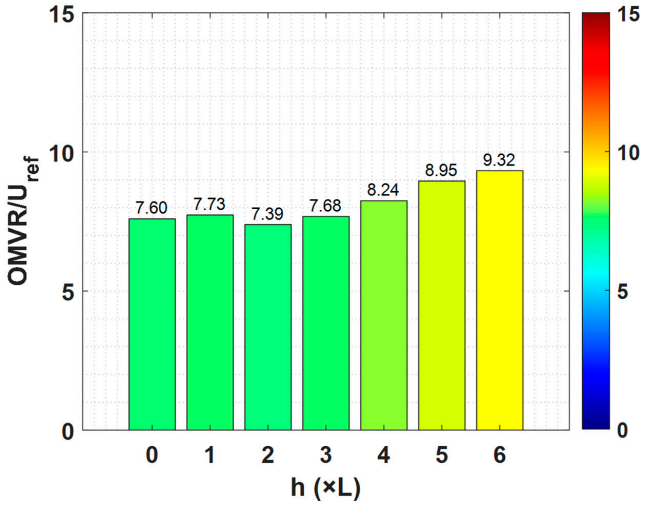


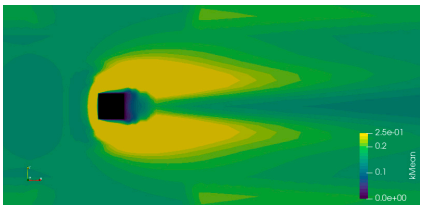
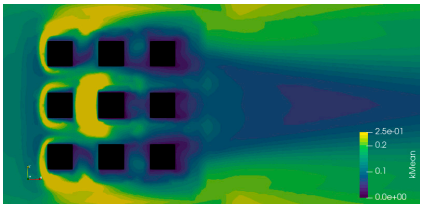
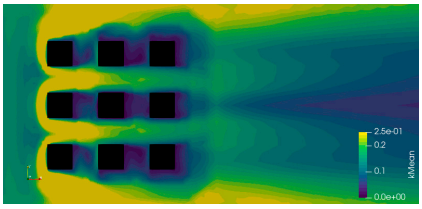
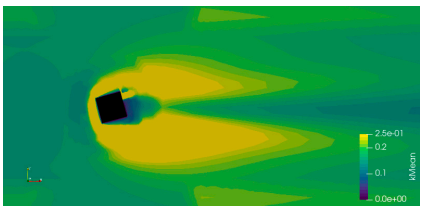
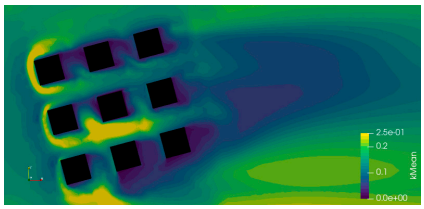
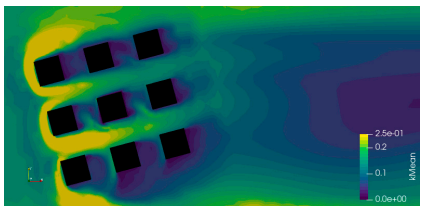
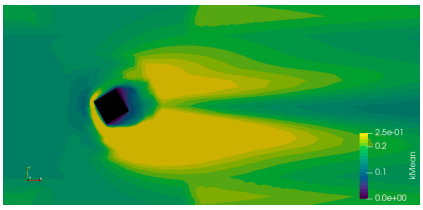
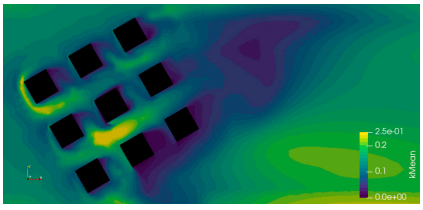
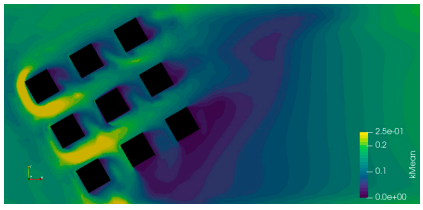
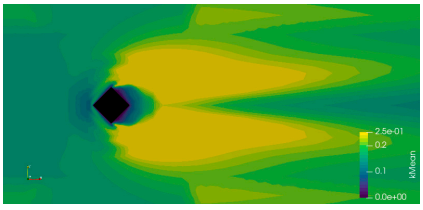
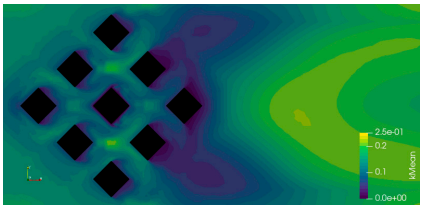
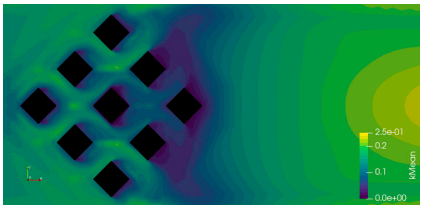
Figure 10. OMVR criterion for all neighborhood configurations.

Among all configurations, the case h = 2L yielded the most favorable OMVR result, categorized as "tolerable". This suggests that buildings of intermediate height strike a balance between insufficient wind deflection (as seen in h = 1L) and excessive channeling (observed for $h \geq$ 3L). As building height increases beyond this point, OMVR continues to rise, with the h = 6L case reaching a peak value of OMVR/U_{ref} = 9.32. These results suggest that building height plays a significant role in pedestrian wind comfort and should be considered during early stages of urban design. Nonetheless, further studies are needed to confirm this trend under more realistic and diverse conditions.

5.4. Other Physical Phenomena

The pedestrian comfort criteria assessed in this study are directly related to intrinsic physical phenomena of wind flow. Two key flow characteristics associated with this relationship are the TKE and vorticity fields. Table 3 presents the TKE fields for the critical cases h = 0L, 2L, and 6L, including average TKE within the neighborhood perimeter. To ensure better visual comparison across cases, the TKE scale was kept constant in the range $[0, 2.5\times 10^{-1}]$ m^2/s.

Table 3. TKE field for the critical cases.

θ	h = 0L	h = 2L	h = 6L
0°			
	$k_{ave} = 1.66 \times 10^{-1}$ m^2/s	$k_{ave} = 1.11 \times 10^{-1}$ m^2/s	$k_{ave} = 1.21 \times 10^{-1}$ m^2/s
15°			
	$k_{ave} = 2.04 \times 10^{-1}$ m^2/s	$k_{ave} = 9.58 \times 10^{-2}$ m^2/s^2	$k_{ave} = 1.13 \times 10^{-1}$ m^2/s
30°			
	$k_{ave} = 1.17 \times 10^{-1}$ m^2/s	$k_{ave} = 8.87 \times 10^{-2}$ m^2/s^2	$k_{ave} = 1.08 \times 10^{-1}$ m^2/s
45°			
	$k_{ave} = 9.88 \times 10^{-2}$ m^2/s^2	$k_{ave} = 7.70 \times 10^{-2}$ m^2/s^2	$k_{ave} = 8.86 \times 10^{-2}$ m^2/s^2

When comparing the isolated building cases to those with surrounding buildings, it is observed that for h = 0L, the yellow regions (representing TKE peaks) are more prominent. Furthermore, as illustrated in Figure 11, the case without neighboring buildings shows less TKE dissipation. This observation suggests a possible correlation between high MVR peaks and elevated TKE levels. The absence of nearby buildings appears to hinder TKE dissipation, making it more pronounced in such configurations. The average values, k_{ave} shown in Table 3, confirm that TKE levels are generally higher without neighboring structures, especially for θ = 15°. With the addition of a shorter height, TKE peaks become less prominent, and dissipation improves, particularly in front of the central building (see Figure 11b). However, as the height of the surroundings increases and flow channeling intensifies, TKE dissipation becomes less intense. Figure 11c shows that dissipation tends to occur laterally along Streets #1 and #2. In this section, all physical parameters are visualized on an X–Y plane located at a cutting height of z = 0.075L.



(**a**) (**b**) (**c**)

Figure 11. TKE dissipation for cases h = (**a**) 0L, (**b**) 2L, and (**c**) 6L.

This effect (taller surrounding buildings channeling the flow through canyons aligned with the predominant wind direction) can be further explored by analyzing the vorticity field along the X-Y plane presented in Table 4. Comparing θ = 0° and 15°, downstream recirculation is more evident for h = 6L, where aligned canyons exhibit low vorticity and primarily serve as flow conduits. For h = 2L, channeling also occurs, though less intensely, and slight recirculation can be observed within the canyons.

Table 4. Vorticity field in X-Y plane for the critical cases.

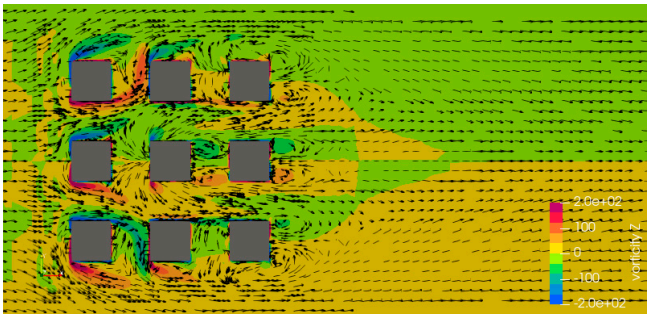
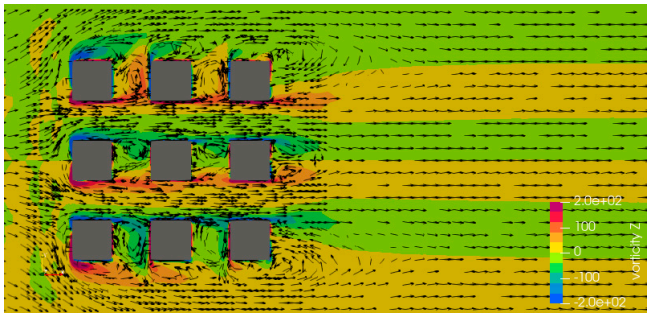
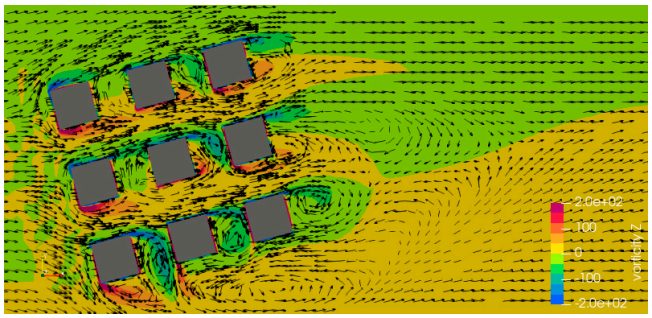
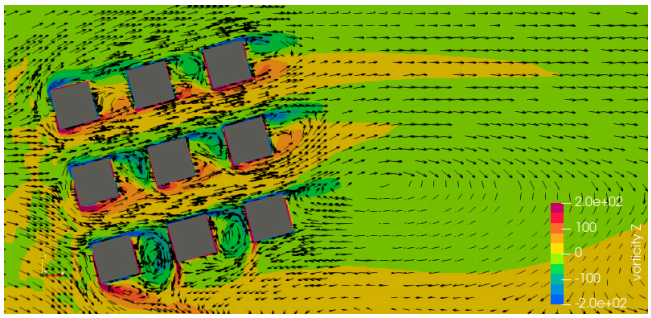
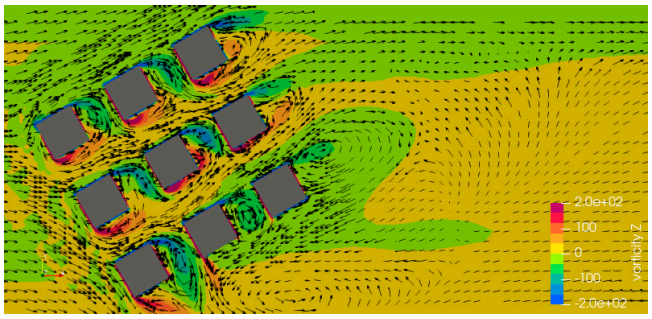
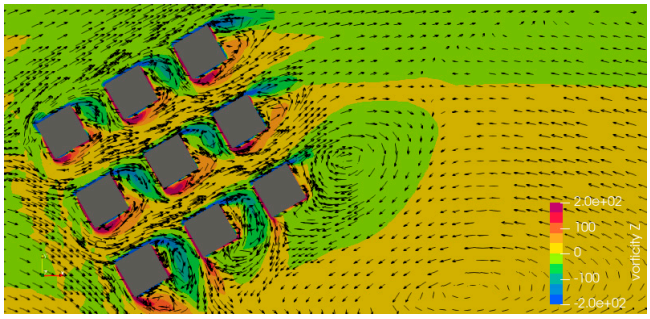
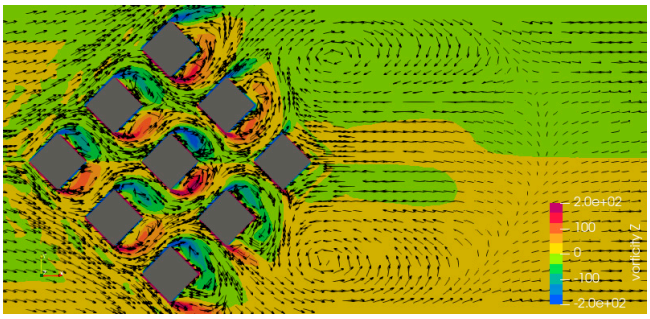
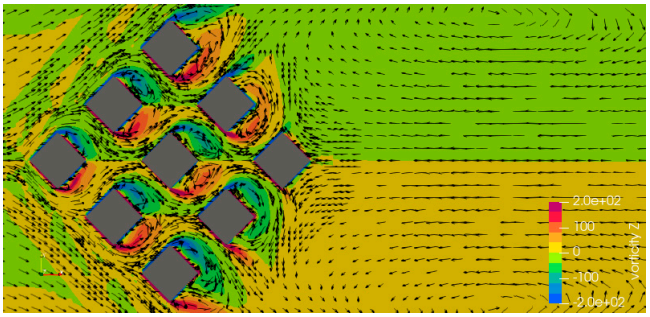
θ	h = 2L	h = 6L
0°		
15°		

Table 4. *Cont.*

θ	h = 2L	h = 6L
30°		
45°		

At θ = 30° and 45°, vorticity becomes more prominent inside the neighborhood, promoting recirculation. Consequently, flow channeling is obstructed, and lower MVR values are generally observed. Therefore, pedestrian comfort criteria should not be analyzed in isolation. Additional flow parameters can help elucidate these mechanisms and contribute to the design of urban spaces that promote greater comfort in public spaces.

6. Conclusions

This study presented a numerical investigation of pedestrian wind comfort within an idealized urban neighborhood consisting of nine buildings. Using Computational Fluid Dynamics (CFD) simulations, the influence of surrounding building height variations (from 0L to 6L) and multiple wind incidence angles (ranging from 0° to 45° at 15° intervals) was systematically examined at pedestrian level, based on the Mean Velocity Ratio (MVR) and Overall Mean Velocity Ratio (OMVR) criteria.

The results showed a marked sensitivity of pedestrian wind comfort to both urban geometry and wind direction. Wind angles aligned with the urban canyons (0° and 15°) intensified the Venturi effect, leading to significantly increased wind speeds between buildings and generating MVR values classified as intolerable or even hazardous.

Conversely, an oblique wind incidence of 45° tended to yield a more uniform airflow distribution, reducing peak velocities and improving comfort. Regarding building height, increasing the height of surrounding structures generally amplified the channeling effect, producing higher mean wind speeds within the canyons. Additionally, the case with no surrounding buildings (h = 0L) was not free from adverse effects, as flow separation around the isolated structure could lead to local velocity peaks surpassing those observed in denser urban configurations.

The findings of this study are consistent with those reported in other works in the field. For example, Pancholy et al. [55] used steady RANS CFD to study pedestrian-level wind comfort in uniform and non-uniform street canyons, finding increased street width raised discomfort, while step-up canyons kept nearly all pedestrian areas within comfort

zones. Kim et al. [56] used LES simulations to assess tall-building effects on pedestrian-level flow and pollutant dispersion, finding that greater height increases mean wind speed and decreases pollutant concentration, with diminishing changes at higher heights, driven by coherent flow structures shaping spatiotemporal pollutant variation.

Overall, the findings suggest that aerodynamic interactions in urban environments are complex, and oversimplified planning assumptions may result in pedestrian-level conditions that are uncomfortable or even unsafe. The spatial arrangement and height of buildings, along with their orientation relative to prevailing winds, should be carefully considered in early-stage urban design. This study underscores the value of CFD-based wind engineering analysis to support the development of safer and more comfortable public spaces.

Limitations of the Research and Recommendations for Future Work

The authors acknowledge that the methodology adopted in this study presents limitations that contextualize the scope of its conclusions. The analysis was based on a simplified, hypothetical urban configuration composed of perfectly aligned buildings with identical base dimensions. Although this idealized layout was instrumental in isolating specific aerodynamic behaviors, it inherently favors certain flow patterns and fails to represent the irregular geometries commonly found in real urban environments, especially in unplanned cities.

Moreover, the evaluation was restricted to four central streets, selected to represent dominant flow orientations. While adequate for initial comparisons, this selection does not capture the full spatial variability of more complex urban morphologies. Future studies aiming at broader generalizability should consider adopting dimensionless morphological parameters. Indices such as the plan area ratio and frontal area ratio have demonstrated strong correlations with pedestrian-level wind speeds, as shown in works by Ramponi and Blocken [57], Ramponi et al. [58], and Tsichritzis and Nikolopoulou [59]. Incorporating such indices would allow analyses to move beyond case-specific scenarios and toward more broadly applicable urban planning guidelines. Future research should also be directed toward the study of thermal comfort, such as Jamei and Rajagopalan [60], who used ENVI-met simulations to study Melbourne's City North, finding that higher aspect ratios, strategic orientation, reduced sky view factor, and shading improved daytime thermal comfort, highlighting the importance of climate-conscious urban design.

The use of the RANS k-ε turbulence model also imposes limitations. Despite its computational efficiency, this model provides time-averaged results and does not resolve transient phenomena such as gusts or peak velocities, which may be relevant for assessing safety and comfort. To better capture such effects, future investigations could explore advanced turbulence models, such as RANS k-ω Shear Stress Transport or Large Eddy Simulations (LES).

Finally, the study was not anchored to a specific geographic location and therefore did not employ meteorological or statistical data related to wind speeds and directions. The assumption of equal probabilities for four wind directions does not reflect typical atmospheric behavior. Future research should prioritize site-specific analyses, incorporating local meteorological data and wind roses to define realistic boundary conditions. Such refinements would significantly enhance the applicability and robustness of the findings.

Author Contributions: P.U.d.S.: conceptualization, software, validation, formal analysis, investigation, resources, data curation, writing—original draft preparation, and visualization. G.B.: conceptualization, methodology, investigation, writing—review and editing, supervision, and project administration. M.G.: resources, writing—review and editing, supervision, and project administration. All authors have read and agreed to the published version of the manuscript.

Funding: Fundação de Coordenação de Aperfeiçoamento de Pessoal de Nível Superior (CAPES)—Finance Code 001 and Conselho Nacional de Desenvolvimento Científico e Tecnológico (CNPq)—302119/2022-1.

Data Availability Statement: The original data presented in the study are openly available in https://github.com/p-ulisses/openfoam-buildings-1-1-6-k-epsilon/ as a minimum dataset to run the files in OpenFOAM v12.

Acknowledgments: The authors would like to thank Fundação de Coordenação de Aperfeiçoamento de Pessoal de Nível Superior (CAPES) and the Conselho Nacional de Desenvolvimento Científico e Tecnológico (CNPq) for funding this work.

Conflicts of Interest: The authors declare no conflicts of interest.

Abbreviations

The following abbreviations are used in this manuscript:

ABL	Atmospheric Boundary Layer
CFD	Computational Fluid Dynamics
FB	Fractional Bias
GAMG	Geometric Agglomeration Multi-Grid
LES	Large-Eddy Simulation
MAE	Mean Absolute Error
MVR	Mean Velocity Ratio
OMVR	Overall Mean Velocity Ratio
RNG	Re-Normalization Group
RANS	Reynolds-Averaged Navier–Stokes
RSM	Reynolds Stress Models
RMSE	Root Mean Square Error
SGS	SubGrid-Scale
TKE	Turbulent Kinetic Energy

Appendix A

This appendix presents tables detailing the streamlines for each numerical simulation case, alongside a plot of the MVR pedestrian Comfort criterion traced along the streets, referencing the axes defined in Figure 4. In total, it consists of seven tables, A1 through A7. Each table corresponds to a specific neighborhood height h and contains the results for all wind incidence angles for that configuration. The tables are organized in ascending order of h, all streamlines are visualized at a slice plane of z = 0.0075L.

Table A1. MVR criteria for cases $h = 0$L.

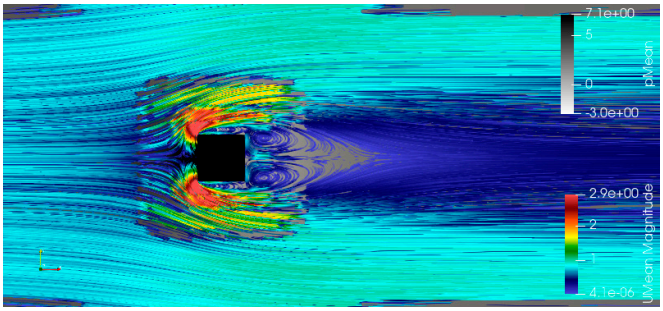
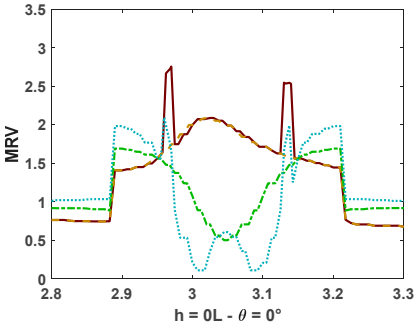
θ	Velocity Field	MVR Criteria
0°	 $y^+_{ave} = 16.2$ $y^+_{max} = 71.1$ $y^+_{min} = 0.74$	

Table A1. *Cont.*

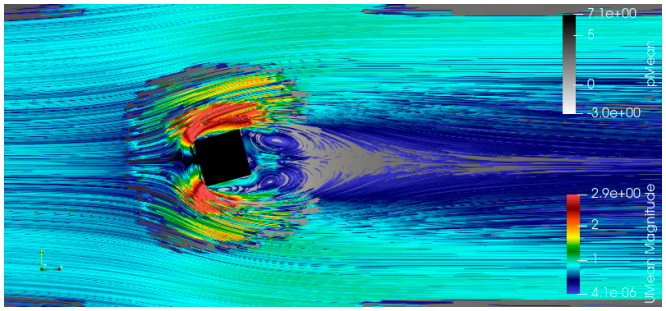
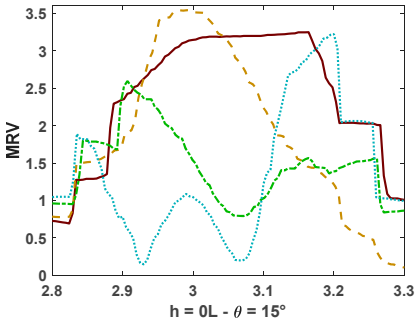
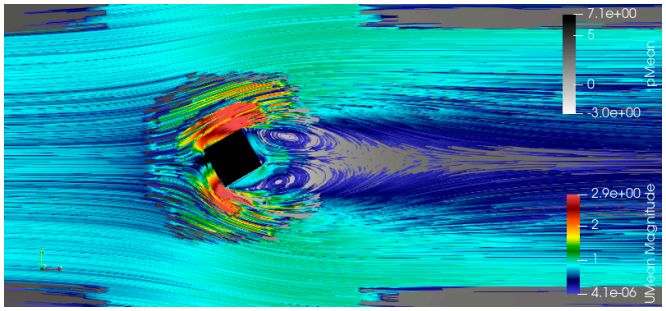
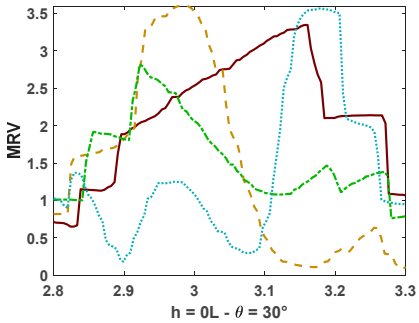
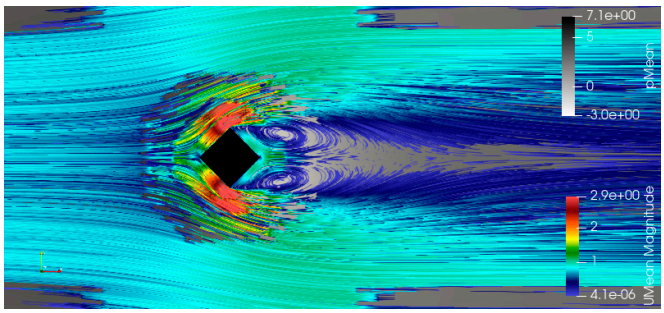
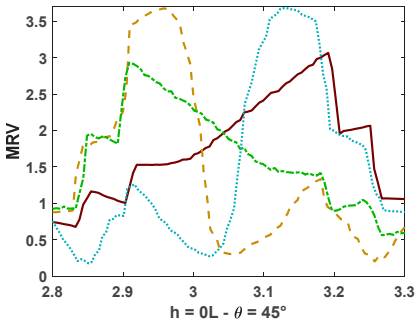
θ	Velocity Field	MVR Criteria
15°		
	$y^+_{ave} = 14.7 \quad y^+_{max} = 103 \quad y^+_{min} = 0.16$	
30°		
	$y^+_{ave} = 10.4 \quad y^+_{max} = 73.8 \quad y^+_{min} = 0.17$	
45°		
	$y^+_{ave} = 8.89 \quad y^+_{max} = 57.84 \quad y^+_{min} = 0.26$	
		

Table A2. MVR criteria for cases $h = 1L$.

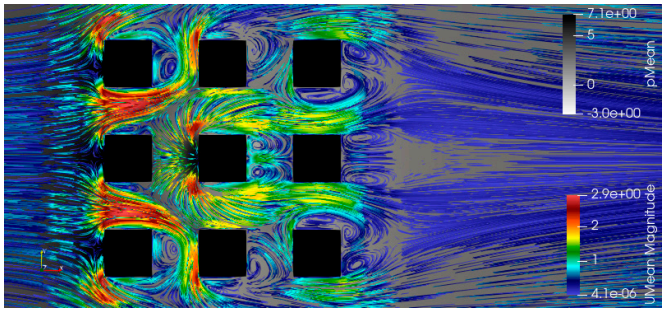
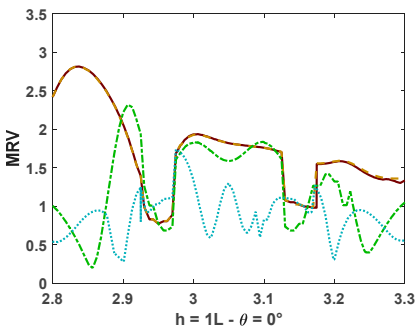
θ	Velocity Field	MVR Criteria
0°		
	$y^+_{ave} = 18.8 \quad y^+_{max} = 72.8 \quad y^+_{min} = 2.84$	

Table A2. *Cont.*

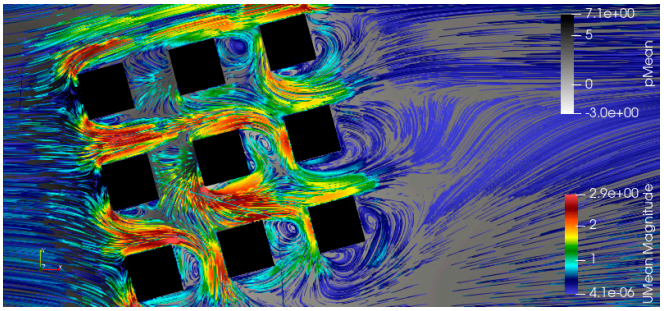
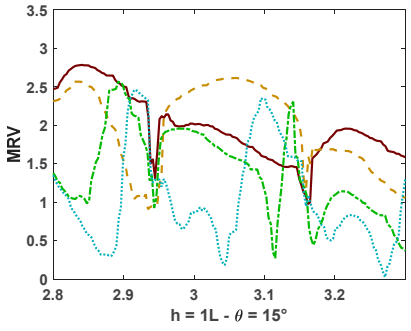
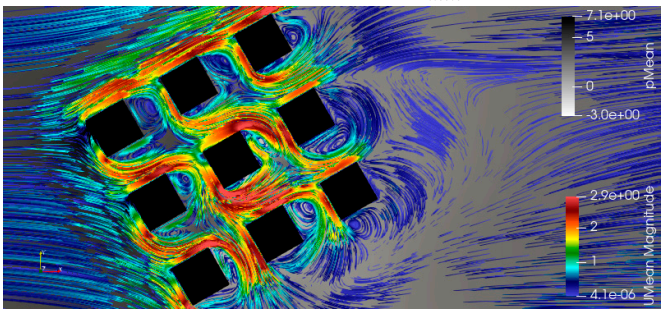
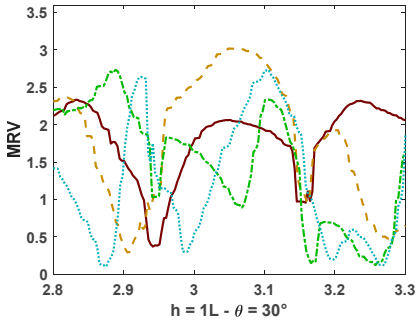
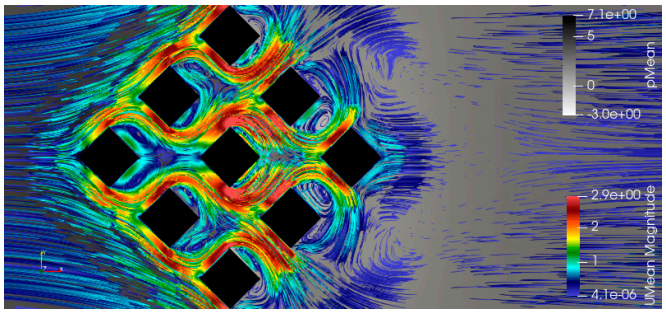
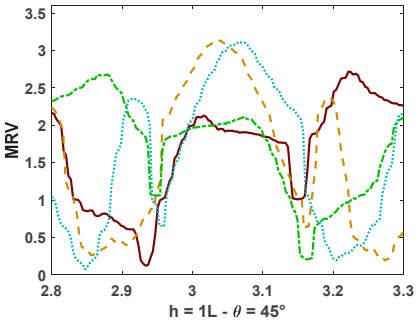
θ	Velocity Field	MVR Criteria
15°		
	$y^+_{ave} = 17.7 \quad y^+_{max} = 95.7 \quad y^+_{min} = 1.27$	
30°		
	$y^+_{ave} = 14.8 \quad y^+_{max} = 79.5 \quad y^+_{min} = 1.45$	
45°		
	$y^+_{ave} = 14.0 \quad y^+_{max} = 74.2 \quad y^+_{min} = 1.52$	
		

Table A3. MVR criteria for cases $h = 2L$.

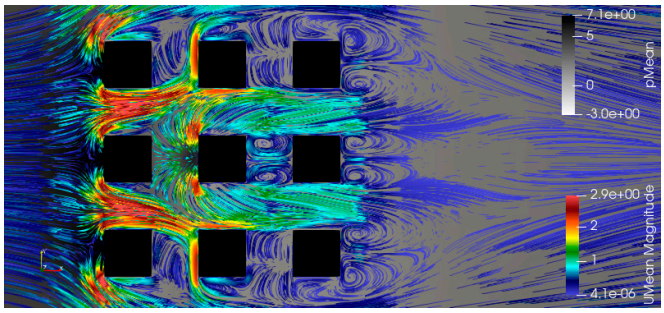
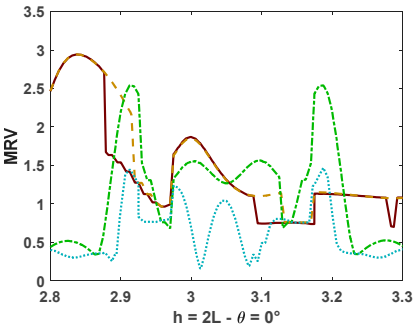
θ	Velocity Field	MVR Criteria
0°		
	$y^+_{ave} = 20.6 \quad y^+_{max} = 88.7 \quad y^+_{min} = 2.07$	

Table A3. *Cont.*

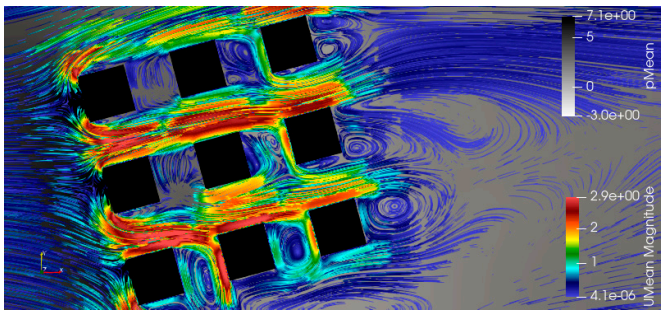
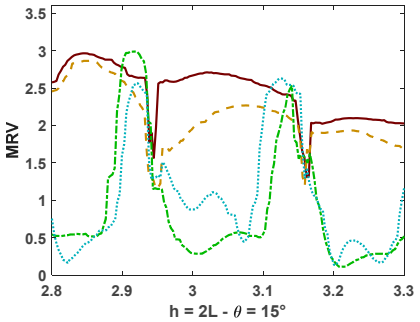
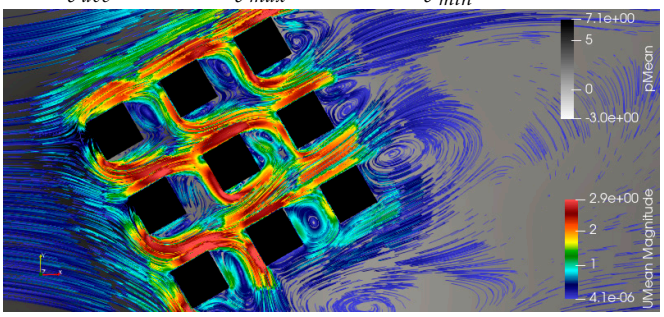
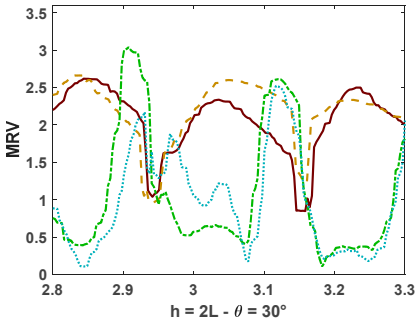
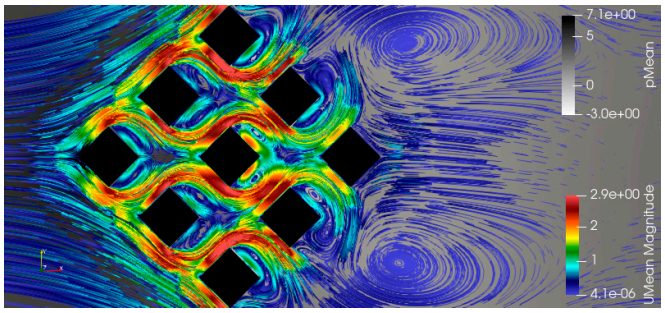
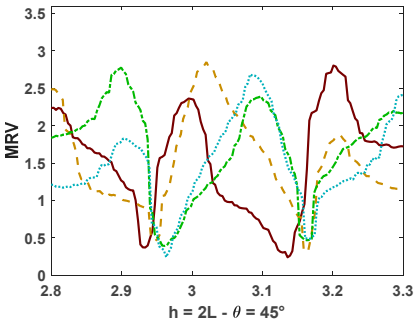
θ	Velocity Field	MVR Criteria
15°	 $y^+_{ave} = 19.0 \quad y^+_{max} = 117.3 \quad y^+_{min} = 0.41$	
30°	 $y^+_{ave} = 14.5 \quad y^+_{max} = 83.3 \quad y^+_{min} = 0.99$	
45°	 $y^+_{ave} = 12.7 \quad y^+_{max} = 74.2 \quad y^+_{min} = 1.41$	
		

Table A4. MVR criteria for cases $h = 3L$.

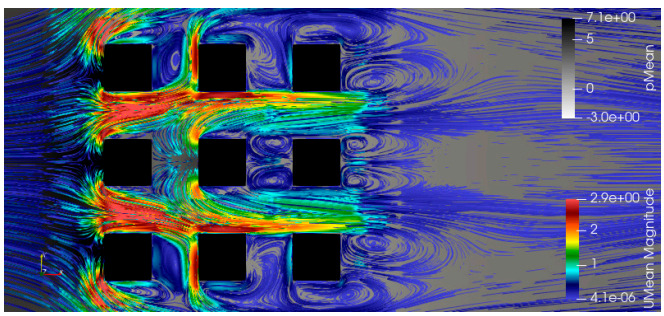
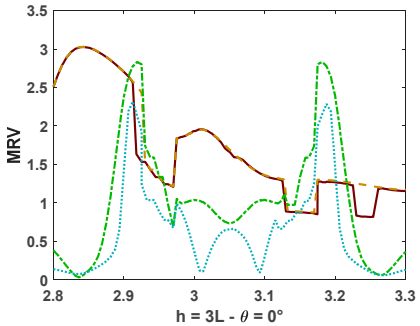
θ	Velocity Field	MVR Criteria
0°	 $y^+_{ave} = 19.7 \quad y^+_{max} = 84.7 \quad y^+_{min} = 3.22$	

Table A4. *Cont.*

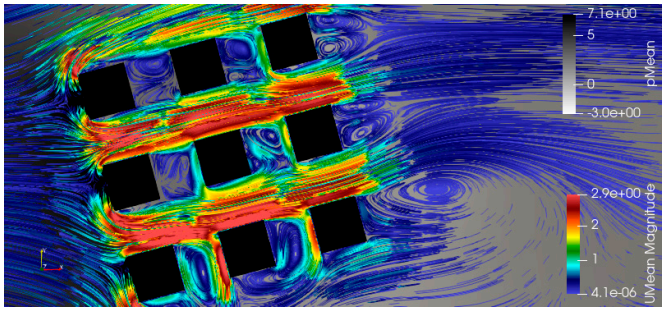
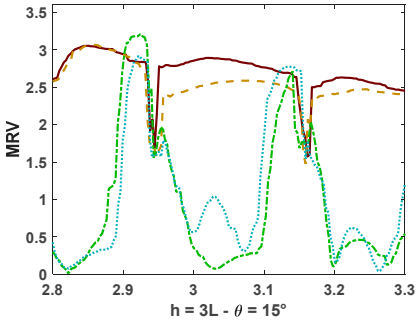
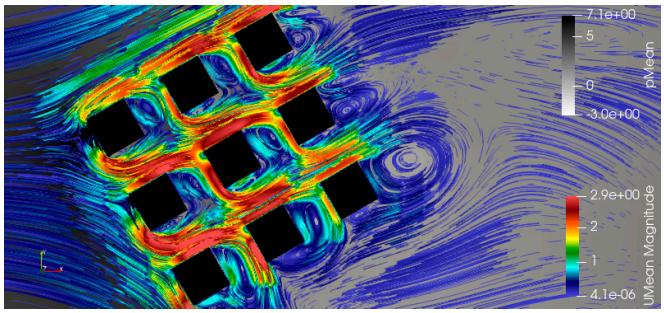
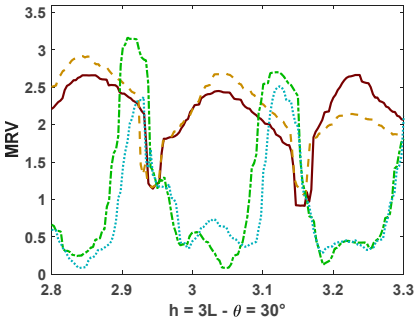
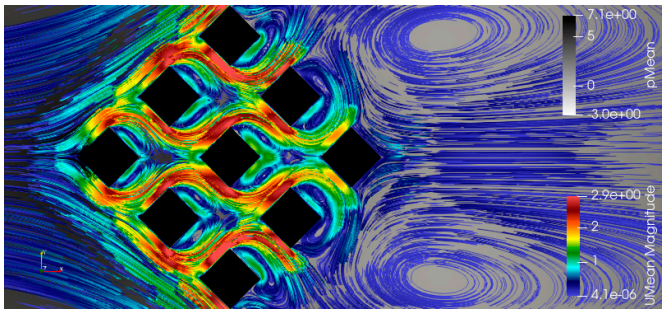
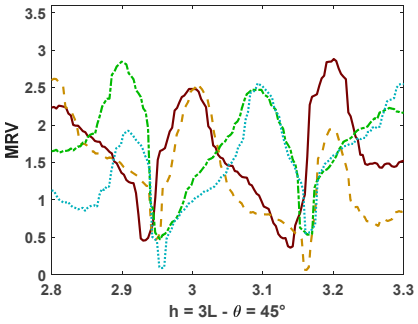
θ	Velocity Field	MVR Criteria
15°		
	$y^+_{ave} = 17.9 \quad y^+_{max} = 109.6 \quad y^+_{min} = 1.11$	
30°		
	$y^+_{ave} = 14.4 \quad y^+_{max} = 85.7 \quad y^+_{min} = 0.97$	
45°		
	$y^+_{ave} = 13.2 \quad y^+_{max} = 87.8 \quad y^+_{min} = 0.74$	
		

Table A5. MVR criteria for cases $h = 4L$.

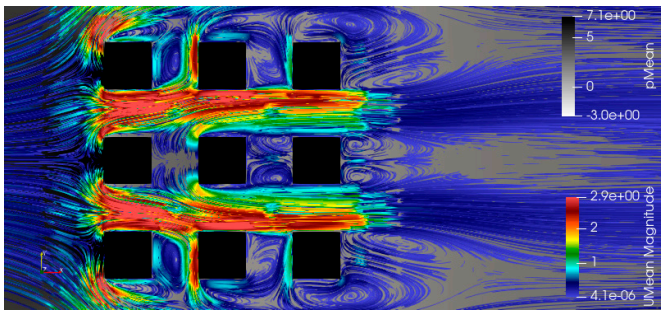
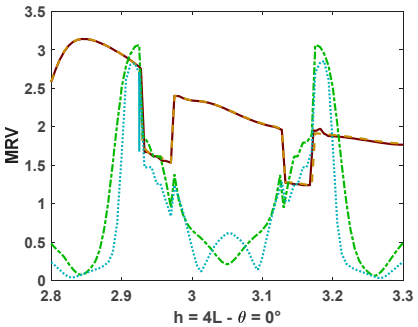
θ	Velocity Field	MVR Criteria
0°		
	$y^+_{ave} = 19.6 \quad y^+_{max} = 88.6 \quad y^+_{min} = 2.29$	

Table A5. *Cont.*

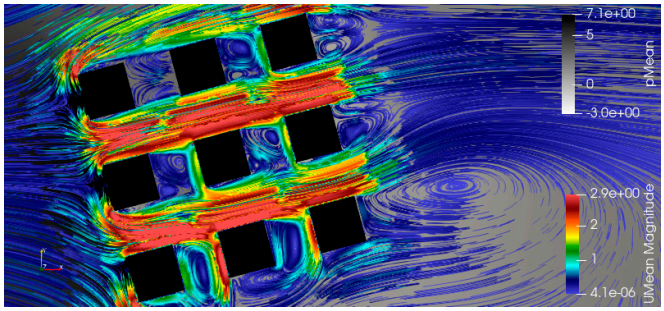
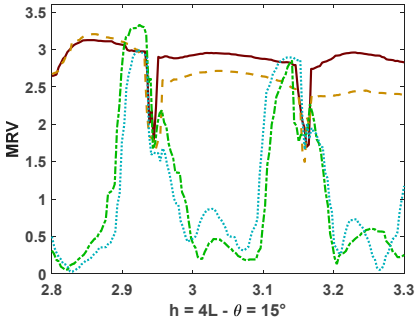
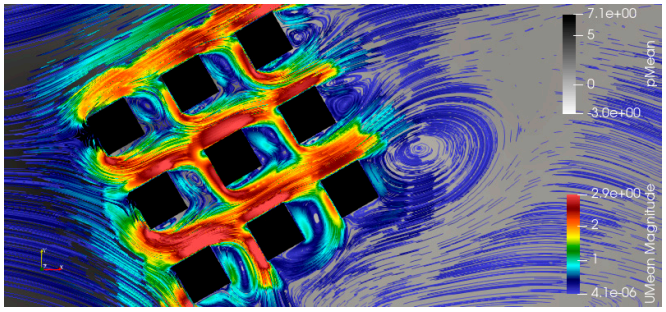
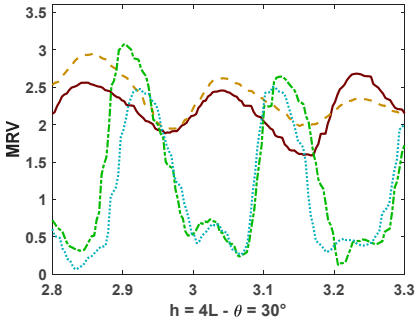
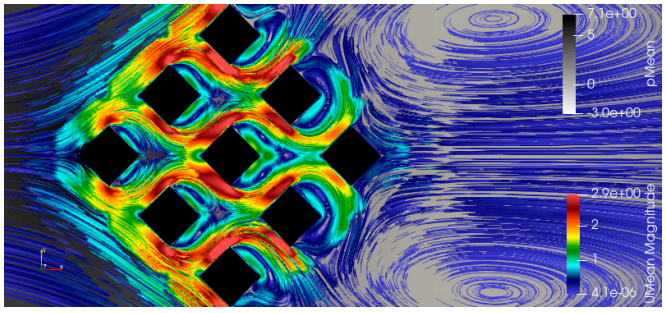
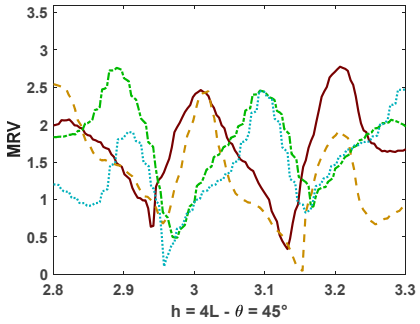
θ	Velocity Field	MVR Criteria
15°	 $y^+_{ave} = 17.8 \quad y^+_{max} = 113.5 \quad y^+_{min} = 0.98$	
30°	 $y^+_{ave} = 19.1 \quad y^+_{max} = 129.8 \quad y^+_{min} = 0.75$	
45°	 $y^+_{ave} = 14.8 \quad y^+_{max} = 104.9 \quad y^+_{min} = 2.46$	
		

Table A6. MVR criteria for cases $h = 5L$.

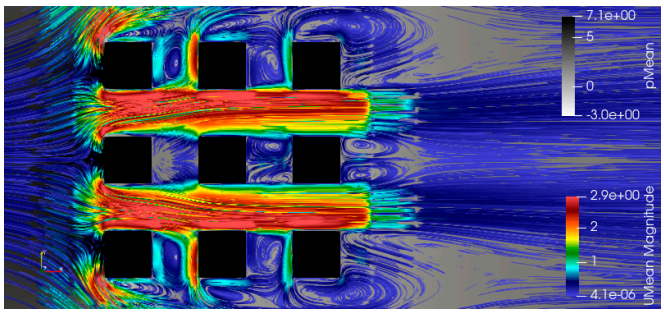
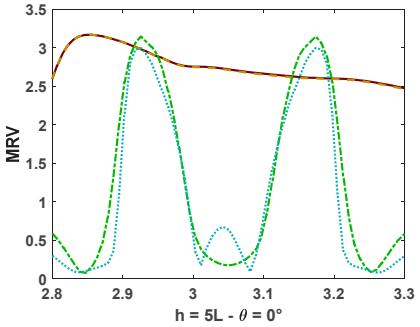
θ	Velocity Field	MVR Criteria
0°	 $y^+_{ave} = 23.5 \quad y^+_{max} = 115.3 \quad y^+_{min} = 3.77$	

Table A6. *Cont.*

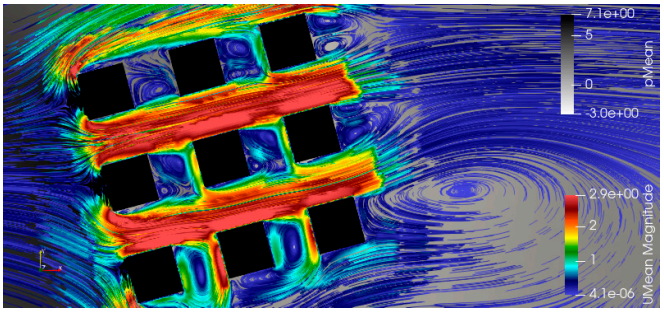
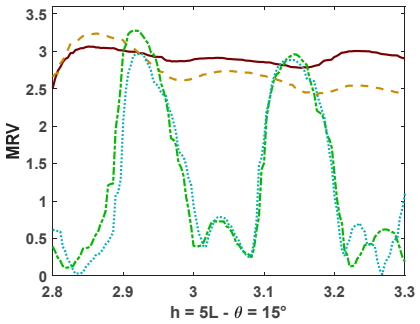
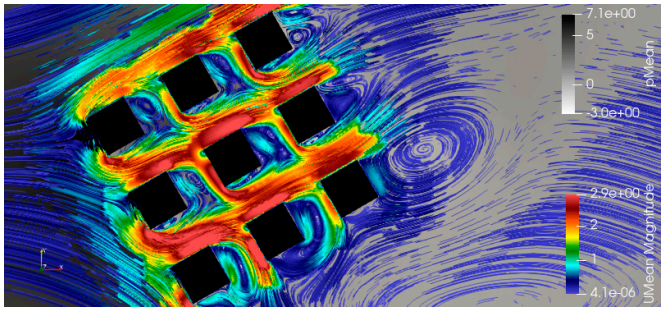
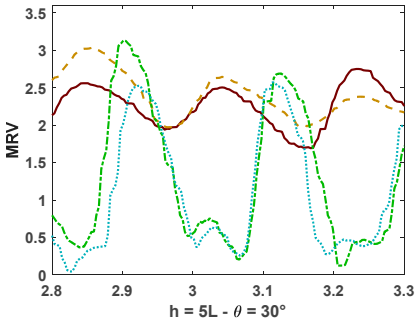
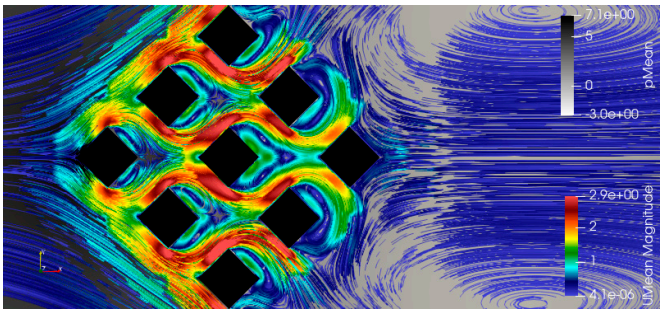
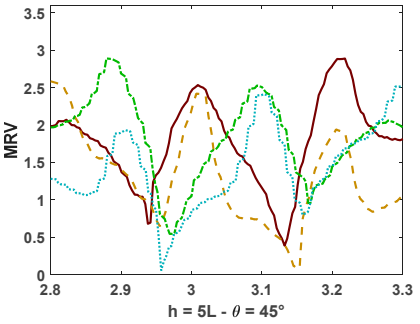
θ	Velocity Field	MVR Criteria
15°	 $y^+_{ave} = 20.6 \quad y^+_{max} = 124.9 \quad y^+_{min} = 1.59$	
30°	 $y^+_{ave} = 17.9 \quad y^+_{max} = 117.8 \quad y^+_{min} = 1.25$	
45°	 $y^+_{ave} = 14.7 \quad y^+_{max} = 103.9 \quad y^+_{min} = 2.44$	
		

Table A7. MVR criteria for cases $h = 6L$.

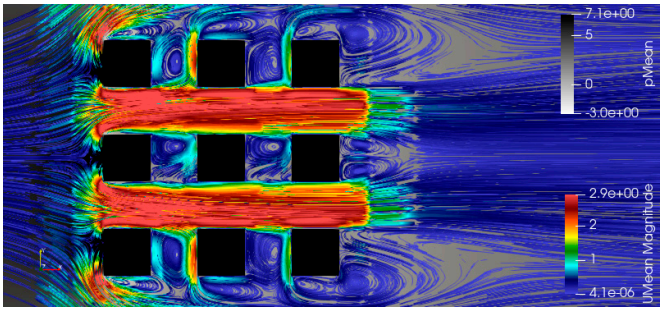
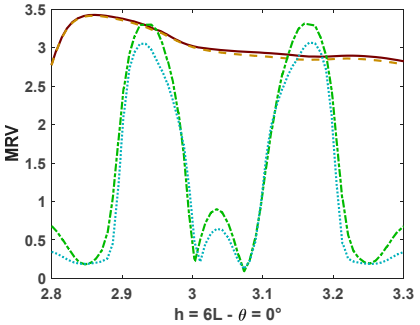
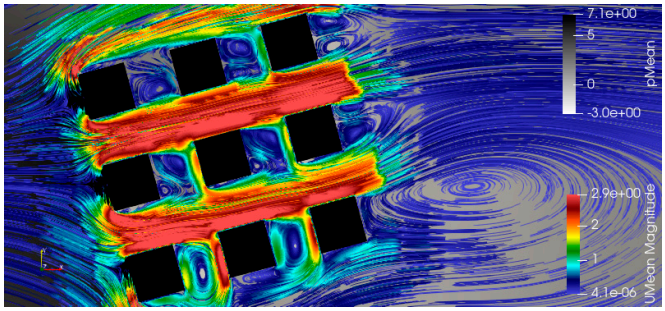
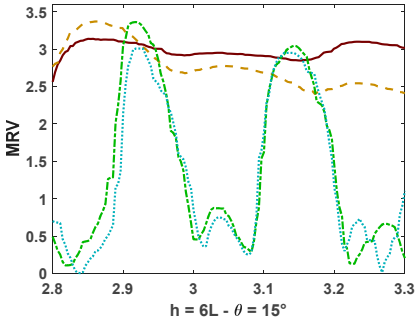
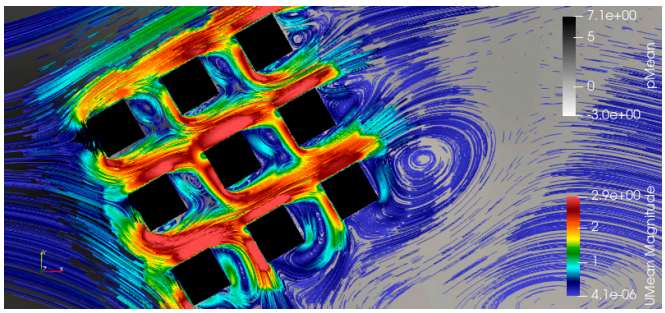
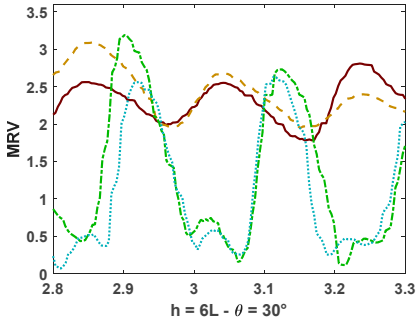
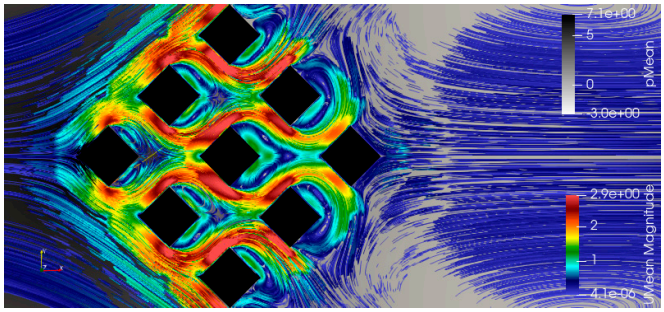
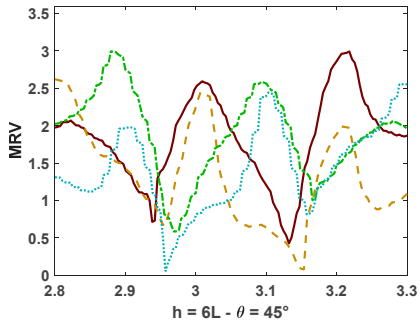
θ	Velocity Field	MVR Criteria
0°	 $y^+_{ave} = 25.2 \quad y^+_{max} = 119.0 \quad y^+_{min} = 3.83$	

Table A7. *Cont.*

θ	Velocity Field	MVR Criteria
15°		
	$y^+_{ave} = 21.2 \quad y^+_{max} = 119.6 \quad y^+_{min} = 1.44$	
30°		
	$y^+_{ave} = 19.1 \quad y^+_{max} = 130.7 \quad y^+_{min} = 1.15$	
45°		
	$y^+_{ave} = 15.5 \quad y^+_{max} = 112.5 \quad y^+_{min} = 1.78$	



References

1. Amerio, A.; Brambilla, A.; Morganti, A.; Aguglia, A.; Bianchi, D.; Santi, F.; Costantini, L.; Odone, A.; Costanza, A.; Signorelli, C.; et al. COVID-19 Lockdown: Housing Built Environment's Effects on Mental Health. *Int. J. Environ. Res. Public Health* **2020**, *17*, 5973. [CrossRef] [PubMed]
2. Millán-Jiménez, A.; Herrera-Limones, R.; López-Escamilla, Á.; López-Rubio, E.; Torres-García, M. Confinement, Comfort and Health: Analysis of the Real Influence of Lockdown on University Students during the COVID-19 Pandemic. *Int. J. Environ. Res. Public Health* **2021**, *18*, 5572. [CrossRef] [PubMed]
3. Met Office. Urban Heat Island Introduction. Available online: https://www.metlink.org/fieldwork-resource/urban-heat-island-introduction/ (accessed on 2 June 2025).
4. Liu, Z.; Zheng, C.; Lu, D.; Wang, Y.; Chen, Y.; Jin, Z.; Zhang, Z. Effects of Wind Shields on Pedestrian-Level Wind Environment around Outdoor Platforms of a Megatall Building. *Atmosphere* **2024**, *15*, 171. [CrossRef]
5. Hashemi, S.; Ghaffarianhoseini, A.; Ghaffarianhoseini, A.; Naismith, N.; Santamouris, M.; Kikumoto, H. Pedestrian-Level Wind Speed Analysis: A Case Study. *Archit. Sci. Rev.* **2024**, *68*, 323–338. [CrossRef]

6. Liu, F.; Ren, Y.; Zhang, L.; Li, X. Impact of Super High-Rise Buildings on Wind Comfort and Safety of Pedestrian Wind Environment: A Case Study in Shanghai, China. Case Stud. *Therm. Eng.* **2025**, *71*, 106197. [CrossRef]
7. Shi, X.; Zhu, Y.; Duan, J.; Shao, R.; Wang, J. Assessment of Pedestrian Wind Environment in Urban Planning Design. *Landsc. Urban Plan.* **2015**, *140*, 17–28. [CrossRef]
8. Chen, L.; Mak, C.M. Integrated Impacts of Building Height and Upstream Building on Pedestrian Comfort around Ideal Lift-Up Buildings in a Weak Wind Environment. *Build. Environ.* **2021**, *200*, 107963. [CrossRef]
9. Du, Y.; Mak, C.M.; Liu, J.; Xia, Q.; Niu, J.; Kwok, K.C.S. Effects of Lift-Up Design on Pedestrian Level Wind Comfort in Different Building Configurations under Three Wind Directions. *Build. Environ.* **2017**, *117*, 84–99. [CrossRef]
10. Nevers, C.; Kubilay, A.; Carmeliet, J.; Derome, D. CFD Simulation of the Wind Flow under Lift-Up Buildings Using a Porous Approach. *Build. Environ.* **2024**, *263*, 111867. [CrossRef]
11. Simões, T.; Estanqueiro, A. A new methodology for urban wind resource assessment. *Renew. Energy* **2016**, *89*, 598–605. [CrossRef]
12. Abohela, I.; Sundararajan, R. Analytical Review of Wind Assessment Tools for Urban Wind Turbine Applications. *Atmosphere* **2024**, *15*, 1049. [CrossRef]
13. Tominaga, Y.; Wang, L.; Zhai, Z.; Stathopoulos, T. Accuracy of CFD simulations in urban aerodynamics and microclimate: Progress and challenges. *Build. Environ.* **2023**, *243*, 110723. [CrossRef]
14. Wijesooriya, K.; Mohotti, D.; Lee, C.-K.; Mendis, P. A technical review of computational fluid dynamics (CFD) applications on wind design of tall buildings and structures: Past, present and future. *J. Build. Eng.* **2023**, *74*, 106828. [CrossRef]
15. Soares, R.C.A.; Silva, P.U.; Bono, G. Estudo Numérico do Conforto Térmico em Arranjo de Edificações com Uso do OpenFOAM. *Mec. Comput.* **2024**, *41*, 7. [CrossRef]
16. Ozsagiroglu, S.; Camci, M.; Taner, T.; Acikgoz, O.; Dalkilic, A.S.; Wongwises, S. CFD analyses on the thermal comfort conditions of a cooled room: A case study. *J. Therm. Anal. Calorim.* **2022**, *147*, 2615–2639. [CrossRef]
17. Rohdin, P.; Moshfegh, B. Numerical predictions of indoor climate in large industrial premises. A comparison between different k–ε models supported by field measurements. *Build. Environ.* **2007**, *42*, 3872–3882. [CrossRef]
18. Yadav, H.; Roy, A.K. Optimization of twisted high-rise building geometries for wind load mitigation and pedestrian comfort. *Asian J. Civ. Eng.* **2025**, *26*, 1595–1620. [CrossRef]
19. Chu, R.; Wang, K. CFD in Urban Wind Resource Assessments: A Review. *Energies* **2025**, *18*, 2626. [CrossRef]
20. Liu, M.; Wang, X. Three-Dimensional Wind Field Construction and Wind Turbine Siting in an Urban Environment. *Fluids* **2020**, *5*, 137. [CrossRef]
21. Guillas, S.; Glover, N.; Malki-Epshtein, L. Bayesian calibration of the constants of the k–ε turbulence model for a CFD model of street canyon flow. *Comput. Methods Appl. Mech. Eng.* **2014**, *279*, 536–553. [CrossRef]
22. Shirzadi, M.; Mirzaei, P.A.; Naghashzadegan, M. Improvement of k-epsilon turbulence model for CFD simulation of atmospheric boundary layer around a high-rise building using stochastic optimization and Monte Carlo Sampling technique. *J. Wind Eng. Ind. Aerodyn.* **2017**, *171*, 366–379. [CrossRef]
23. Houda, S.; Belarbi, R.; Zemmouri, N. A CFD Comsol model for simulating complex urban flow. *Energy Procedia* **2017**, *139*, 373–378. [CrossRef]
24. Zhao, R.; Liu, S.; Liu, J.; Jiang, N.; Chen, Q. Equation discovery of dynamized coefficients in the k-ε model for urban airflow and airborne contaminant dispersion. *Sustain. Cities Soc.* **2023**, *99*, 10488. [CrossRef]
25. Mohotti, D.; Wijesooriya, K.; Dias-da-Costa, D. Comparison of Reynolds Averaging Navier-Stokes (RANS) turbulent models in predicting wind pressure on tall buildings. *J. Build. Eng.* **2019**, *21*, 1–17. [CrossRef]
26. Toja-Silva, F.; Kono, T.; Peralta, C.; Lopez-Garcia, O.; Chen, J. A review of computational fluid dynamics (CFD) simulations of the wind flow around buildings for urban wind energy exploitation. *J. Wind Eng. Ind. Aerodyn.* **2018**, *180*, 66–87. [CrossRef]
27. Blocken, B.; Stathopoulos, T.; van Beeck, J.P.A.J. Pedestrian-level wind conditions around buildings: Review of wind-tunnel and CFD techniques and their accuracy for wind comfort assessment. *Build. Environ.* **2016**, *100*, 50–81. [CrossRef]
28. Toparlar, Y.; Blocken, B.; Maiheu, B.; van Heijst, G.J.F. A review on the CFD analysis of urban microclimate. *Renew. Sustain. Energy Rev.* **2017**, *80*, 1613–1640. [CrossRef]
29. Ricci, A. Review of OpenFOAM applications in the computational wind engineering: From wind environment to wind structural engineering. *Meccanica* **2024**, *60*, 1695–1735. [CrossRef]
30. Aristodemou, E.; Mottet, L.; Constantinou, A.; Pain, C. Turbulent flows and pollution dispersion around tall buildings using adaptive large eddy simulation (LES). *Buildings* **2020**, *10*, 127. [CrossRef]
31. Zheng, X.; Yang, J. CFD simulations of wind flow and pollutant dispersion in a street canyon with traffic flow: Comparison between RANS and LES. *Sustain. Cities Soc.* **2021**, *75*, 103307. [CrossRef]
32. Talwar, T.; Yuan, C. Impact of natural urban terrain on the pedestrian wind environment in neighborhoods: A CFD study with both wind and buoyancy-driven scenarios. *Build. Environ.* **2024**, *261*, 111746. [CrossRef]
33. Acarer, S.; Uyulan, Ç.; Karadeniz, Z.H. Optimization of radial inflow wind turbines for urban wind energy harvesting. *Energy* **2020**, *202*, 117772. [CrossRef]

34. Juan, Y.-H.; Wen, C.-Y.; Chen, W.-Y.; Yang, A.-S. Numerical assessments of wind power potential and installation arrangements in realistic highly urbanized areas. *Renew. Sustain. Energy Rev.* **2021**, *135*, 110165. [CrossRef]
35. Juan, Y.-H.; Wen, C.-Y.; Li, Z.; Yang, A.-S. Impacts of urban morphology on improving urban wind energy potential for generic high-rise building arrays. *Appl. Energy* **2021**, *299*, 117304. [CrossRef]
36. Mirzaei, P.A. CFD modeling of micro and urban climates: Problems to be solved in the new decade. *Sustain. Cities Soc.* **2021**, *69*, 102839. [CrossRef]
37. Li, J.; Guo, F.; Chen, H. A study on urban block design strategies for improving pedestrian-level wind conditions: CFD-based optimization and generative adversarial networks. *Energy Build.* **2024**, *304*, 113863. [CrossRef]
38. Mattar, S.J.; Kavian Nezhad, M.R.; Versteege, M.; Lange, C.F.; Fleck, B.A. Validation process for rooftop wind regime CFD model in complex urban environment using an experimental measurement campaign. *Energies* **2021**, *14*, 2497. [CrossRef]
39. Vita, G.; Salvadori, S.; Misul, D.A.; Hemida, H. Effects of inflow condition on RANS and LES predictions of the flow around a high-rise building. *Fluids* **2020**, *5*, 233. [CrossRef]
40. Associação Brasileira de Normas Técnicas. *NBR 6123: Forças Devidas ao Vento em Edificações*; ABNT: Rio de Janeiro, Brazil, 2023.
41. Blessmann, J. *Ação do Vento em Telhados*, 2nd ed.; Editora da UFRGS: Porto Alegre, Brazil, 2009.
42. Du, Y.; Mak, C.M.; Kwok, K.; Tse, K.-T.; Lee, T.-C.; Ai, Z.; Liu, J.; Niu, J. New criteria for assessing low wind environment at pedestrian level in Hong Kong. *Build. Environ.* **2017**, *123*, 23–36. [CrossRef]
43. Chen, L.; Mak, C.M. Numerical evaluation of pedestrian-level wind comfort around "lift-up" buildings with various unconventional configurations. *Build. Environ.* **2021**, *188*, 107429. [CrossRef]
44. Li, W.; Mak, C.M.; Cai, C.; Fu, Y.; Tse, K.T.; Niu, J. Wind tunnel measurement of pedestrian-level gust wind flow and comfort around irregular lift-up buildings within simplified urban arrays. *Build. Environ.* **2024**, *256*, 111487. [CrossRef]
45. da Silva, P.U.; Bono, G.; Greco, M. Application of Topology Optimization as a Tool for the Design of Bracing Systems of High-Rise Buildings. *Buildings* **2025**, *15*, 1180. [CrossRef]
46. Launder, B.E.; Spalding, D.B. The numerical computation of turbulent flows. *Comput. Methods Appl. Mech. Eng.* **1974**, *3*, 269–289. [CrossRef]
47. Launder, B.E.; Reece, G.J.; Rodi, W. Progress in the development of a Reynolds-stress turbulence closure. *J. Fluid Mech.* **1975**, *68*, 537–566. [CrossRef]
48. El Tahry, S.H. K-epsilon equation for compressible reciprocating engine flows. *J. Energy* **1983**, *7*, 345–353. [CrossRef]
49. Franke, J.; Hirsch, C.; Jensen, A.G.; Krüs, H.W.; Schatzmann, M.; Westbury, P.S.; Miles, S.D.; Wisse, J.A.; Wright, N.G. Recommendations on the use of CFD in wind engineering. In Proceedings of the International Conference on Urban Wind Engineering and Building Aerodynamics, Sint Genesius Rode, Belgium, 5–7 May 2004.
50. Tominaga, Y.; Mochida, A.; Yoshie, R.; Kataoka, H.; Nozu, T.; Masaru, Y.; Shirasawa, T. AIJ guidelines for practical applications of CFD to pedestrian wind environment around buildings. *J. Wind Eng. Ind. Aerodyn.* **2008**, *96*, 1749–1761. [CrossRef]
51. da Silva, P.U. Emprego de Otimização Topológica e DFC no Projeto de Sistemas de Contraventamento em Ambientes Urbanos. Master's Thesis, Universidade Federal de Pernambuco, Caruaru, Brazil, 2022. Available online: https://repositorio.ufpe.br/handle/123456789/47230 (accessed on 4 June 2025).
52. Liu, X.; Niu, J.; Kwok, K.C.S. Evaluation of RANS turbulence models for simulating wind-induced mean pressures and dispersions around a complex-shaped high-rise building. *Build. Simul.* **2013**, *6*, 151–164. [CrossRef]
53. Liu, J.; Niu, J. CFD simulation of the wind environment around an isolated high-rise building: An evaluation of SRANS, LES and DES models. *Build. Environ.* **2016**, *96*, 91–106. [CrossRef]
54. New Frontier of Education and Research in Wind Engineering Proposed by School of Architecture and Wind Engineering at the Tokyo Polytechnic University. Available online: http://www.wind.arch.t-kougei.ac.jp/system/eng/contents/code/tpu (accessed on 9 June 2025).
55. Pancholy, P.P.; Clemens, K.; Geoghegan, P.; Jermy, M.; Moyers-Gonzalez, M.; Wilson, P.L. Numerical study of flow structure and pedestrian-level wind comfort inside urban street canyons. *J. R. Soc. N. Z.* **2021**, *51*, 307–332. [CrossRef]
56. Kim, J.-W.; Baik, J.-J.; Han, B.-S.; Lee, J.; Jin, H.-G.; Park, K.; Yang, H.; Park, S.-B. Tall-building effects on pedestrian-level flow and pollutant dispersion: Large-eddy simulations. *Atmos. Pollut. Res.* **2022**, *13*, 101500. [CrossRef]
57. Ramponi, R.; Blocken, B. A Computational Study on the Influence of Urban Morphology on Wind-Induced Outdoor Ventilation. In Proceedings of the International Congress on Environmental Modelling and Software, Leipzig, Germany, 1 July 2012.
58. Ramponi, R.; Blocken, B.; de Coo, L.B.; Janssen, W.D. CFD simulation of outdoor ventilation of generic urban configurations with different urban densities and equal and unequal street widths. *Build. Environ.* **2015**, *92*, 152–166. [CrossRef]

59. Tsichritzis, L.; Nikolopoulou, M. The effect of building height and façade area ratio on pedestrian wind comfort of London. *J. Wind Eng. Ind. Aerodyn.* **2019**, *191*, 63–75. [CrossRef]
60. Jamei, E.; Rajagopalan, P. Effect of street design on pedestrian thermal comfort. *Archit. Sci. Rev.* **2019**, *62*, 92–111. [CrossRef]

Disclaimer/Publisher's Note: The statements, opinions and data contained in all publications are solely those of the individual author(s) and contributor(s) and not of MDPI and/or the editor(s). MDPI and/or the editor(s) disclaim responsibility for any injury to people or property resulting from any ideas, methods, instructions or products referred to in the content.